Linköping Studies in Science and Technology
Thesis No. 1529

Modelling of Failure in High Strength Steel Sheets

Oscar Björklund

Linköping University
INSTITUTE OF TECHNOLOGY

LIU–TEK–LIC–2012:14

Department of Management and Engineering, Division of Solid Mechanics
Linköping University,
SE–581 83, Linköping, Sweden
http://www.solid.iei.liu.se/

Linköping, April 2012

Cover:
Results from finite element simulation of a forming limit test.

Printed by:
LiU-Tryck, Linköping, Sweden, 2012
ISBN 978–91–7519–895–5
ISSN 0280–7971

Distributed by:
Linköping University
Department of Management and Engineering
SE–581 83, Linköping, Sweden

This document was prepared with LaTeX, April 30, 2012

Preface

The work presented in this thesis has been carried out at the Division of Solid Mechanics, Linköping University with financial support from the VINOVA PFF project "Fail" and the SFS ProViking project "SuperLight Steel Structures". The industrial partners Dynamore Nordic, Outokumpu Stainless, Saab Automobile, Scania, SSAB, SvereaIVF and Volvo Car Corporation are also gratefully acknowledged for their support.

I would like to thank my supervisor, Professor Larsgunnar Nilsson for all his support and guidance during course of this work. I also greatly appreciate all my colleagues at the Division of Solid Mechanics for their help, in particular Rikard Larsson, Lic. Eng., for all his support and guidance concerning constitutive modelling.

For their assistance during the mechanical testing throughout this project I would like to thank Andreas Lundstedt at Outokumpu Stainless and Bo Skoog, Ulf Bengtsson and Sören Hoff at Linköping University.

I am also grateful to all my friends and my family for their support over the course of all these years. I could not have done it without you.

Oscar Björklund

Linköping, April 2012

"Results! Why, man, I have gotten a lot of results. I know several thousand things that won't work"

Thomas Edison

Abstract

In this theses the high strength steel Docol 600DP and the ultra high strength steel Docol 1200M are studied. Constitutive laws and failure models are calibrated and verified by the use of experiments and numerical simulations. For the constitutive equations, an eight parameter high exponent yield surface has been adopted, representing the anisotropic behaviour, and a mixed isotropic-kinematic hardening has been used to capture non-linear strain paths.

For ductile sheet metals three different failure phenomena have been observed: (i) ductile fracture, (ii) shear fracture, and (iii) instability with localised necking. The models for describing the different failure types have been chosen with an attempt to use just a few tests in addition to these used for the constitutive model. In this work the ductile and shear fracture have been prescribed by models presented by Cockroft-Latham and Bressan-Williams, respectively. The instability phenomenon is described by the constitutive law and the finite element models. The results obtained are in general in good agreement with test results.

The thesis is divided into two main parts. The background, theoretical framework, mechanical experiments and finite element models are presented in the first part. In the second part, two papers are appended.

List of Papers

In this thesis, the following papers have been included:

I. R. Larsson, O. Björklund, L. Nilsson, K. Simonsson (2011). *A study of high strength steels undergoing non-linear strain paths - Experiments and modelling*, Journal of Materials Processing Technology, Volume 211, pp. 122-132.

II. O. Björklund, R. Larsson, L. Nilsson (2012). *Failure of high strength steel sheets - Experiments and modelling*, Submitted.

Own contribution

In the first paper, Rikard Larsson and I jointly performed the modelling and experimental work. However, Rikard Larsson was responsible for writing the paper. In the second paper, the modelling and experimental work were once again performed by Rikard Larsson and myself, but I was responsible for evaluating the failure phenomena and for writing the paper.

Contents

Preface iii

Abstract v

List of Papers vii

Contents ix

Part I Theory and Background

1 Introduction 3

2 Steels 5
2.1 Crystal Structure . . . 6
2.2 Dual Phase Steel . . . 6
2.3 Martensitic Steel . . . 7

3 Deformation and Fracture 9

4 Constitutive Modelling 11
4.1 Isotropic Hardening . . . 12
4.2 Kinematic Hardening . . . 14
4.3 Mixed Hardening . . . 15
4.4 Effective Stress . . . 16

5 Fracture Modelling 19
5.1 Ductile Fracture . . . 22
5.2 Shear Fracture . . . 23
5.3 Phenomenological Fracture Models . . . 23

6 Modelling Instability 29
6.1 Instability in Plane Strain . . . 29
6.2 Analytical Instability Models . . . 31
6.3 The Marciniak and Kuczynski Model . . . 33
6.4 Finite Element Model . . . 35

6.5 Evaluation of Instability 36

7 Mechanical Experiments **39**
7.1 Pre-Deformation 39
7.2 Tensile Test 41
7.3 Simple Shear Test 41
7.4 Plane Strain Test 42
7.5 Balanced Biaxial Test 42
7.6 Nakajima Test 43

8 Finite Element Modelling **45**
8.1 Pre-Straining 46
8.2 Tensile Test 46
8.3 Shear Test 47
8.4 Plane Strain Test 48
8.5 Nakajima Test 50

9 Conclusions and Discussion **51**

10 Review of Appended Papers **53**

Bibliography **55**

Part II Appended Papers

Paper I: A study of high strength steels undergoing non-linear strain paths - Experiments and modelling 63

Paper II: Failure of high strength steel sheets - Experiments and modelling 77

Part I

Theory and Background

1 Introduction

Due to the desire from industries to shorten product development lead time, the use of Simulation Based Design (SBD) is rapidly increasing. The development of finite element (FE) methods and the rapid growth of computational power have made it possible for SBD to advance from research to industrial utilisation. In addition to reduced development time and cost, the possibility of determining the product's properties at an early stages of the design process is of utmost importance e.g. to find out if a car is safe in a crash situation. Simultaneously with the development of SBD, material suppliers have developed more advanced steels with improved mechanical properties. However, these advanced steels often show anisotropic behaviour and more complex hardening compared to traditional low-carbon steels. Consequently, the demand for research on material models, including failure models suitable for these steels, has increased.

The constitutive model that has been used throughout this work includes an eight parameter high exponent yield surface with mixed isotropic-kinematic hardening. The model has the ability to represent the anisotropic behaviour that is shown in mechanical tests, even for a complex loading path. To further increase the ability to predict the product's potential and thereby enable a more optimised product, the necessity of improving failure models has arisen. At present, progressive failure is not included in automotive FE simulations. In order to predict the likelihood of failure, the predicted strain states are compared to experimental forming limit curves (FLC). However, the experimental FLC is constructed for linear strain paths, although its locus has been shown to depend on the strain path. Therefore, the prediction of failure of a component, e.g. a car body part subjected to a crash simulation, lacks information from its previous design history. Thus, an improved phenomenological model for prediction of failure is desired. A phenomenological failure model must have the ability to inherit the properties of a component from its prior manufacturing process.

Macroscopic fractures have always been of great interest. As early as the beginning of 16th century, Leonardo da Vinci explained fractures in terms of mechanical variables. He established that the load an iron wire could carry depended on the length of the wire, as a consequence of the amount of voids in the material. The longer the wire, the more voids, which led to lower load-carrying capacity. Even if material fracture has been studied for a long time, the underlying microscopical fracture mechanisms are hard to translate to a phenomenological model. Since the

underlying mechanisms need to be represented on a length scale, which can be used in an FE simulation, it would be computationally expensive, and hence too time consuming, to represent the fracture on a micromechanical scale. Throughout this work, the expressions failure and fracture are used extensively:

- **Failure** - loss of load-carrying capacity of a component or a structure.
- **Fracture** - material separation into two, or more, pieces.

The term failure incorporates the term fracture but may also be other structural phenomena which do not include a material separation, e.g. material and geometrical instabilities. In ductile sheet metals three different failure phenomena have been observed: (i) ductile fracture, (ii) shear fracture and (iii) material instability with localisation. The third term instability with localisation is also sometimes denoted as purely-plastic failure. In this work the different phenomena have been modelled separately and the focus has been placed on using failure models which can easily be calibrated from simple mechanical tests. For modelling of the ductile and shear fractures the Cockroft-Latham and Bressan-Williams models, respectively, have been used. Each of their models contains only one material parameter and are easy to calibrate. The instability phenomenon is described by the FE model and the constitutive law and needs no further mechanical experimental calibration.

Even if the objective of this project is to identify improved material and failure models suited for high strength sheet metals, the benefit in a longer perspective may be the opportunity to produce lighter and safer structures. The environmental profit of producing lighter products is obvious for the automotive industry, but also other industrial applications can profit from reducing weight i.e. lighter containers will result in an ability to increase the pay-load. The safety of occupants in cars has been an increasingly important marketing issue for the automotive industry. By using new materials to the very edge a more optimised product can be obtained and thereby many fatalities may be prevented.

2 Steels

The classification of different steel grades is often made by the amount and type of alloying substances. However, it is also common to talk about different groups of steels, e.g. High-Strength Low Alloy (HSLA) steel, High-Strength Steel (HSS), Ultra High-Strength Steel (UHSS), Advance High-Strength Steel (AHSS), Dual Phase (DP) Steel, and Transformation-Induced Plasticity (TRIP) Steel. A specific steel can be a part of more than one group as there is no unequivocal division. However, in this work the materials studied are categorised into the two groups HSS and UHSS. These groups are grouped according to the yield strength, and steels with a yield strength between 210 to 550 MPa are classified as HSS and steels with a yield strength over 550 MPa are classified as UHSS, see Opbroek (2009).

The steels covered in this study are Docol 600DP and Docol 1200M. The name Docol is a SSAB trademark. Docol 600DP is an HSS with a dual face structure consisting of about 75% ferrite and 25% martensite, where the two-phase microstructure is produced by heat treatment. Docol 1200M is an UHSS with a fully martensitic steel produced by water quenching from an elevated temperature in the austenitic range, see Olsson et al. (2006). The nominal thicknesses of the steel sheets studied were 1.48 mm and 1.46 mm for Docol 600DP and Docol 1200M, respectively. For details on the chemical composition of the Docol 600DP and Docol 1200M, see Table 1.

Table 1: *Chemical composition of Docol 600DP and Docol 1200M.*

	C [%]	Si [%]	Mn [%]	P [%]	S [%]	Nb [%]	Al [%]	Fe [%]
Docol 600DP	0.10	0.20	1.5	0.01	0.002	-	0.04	balance
Docol 1200M	0.11	0.2	1.6	0.015	0.002	0.015	0.04	balance

2.1 Crystal Structure

The crystal structure of the atoms in a metal is composed of regular three dimensional patterns called a crystal lattice. There are a number of different types of crystal lattices and it is common to talk about unit cells of different types. For metals, the most common types of unit cells are body-centered cubic (BCC), face-centered cubic (FCC), hexagonal close-packed (HCP), and body-centered tetragonal (BCT), see Figure 1. For a more complete overview of different types of unit cells see e.g. Askeland (1998). For pure iron there are three different types of phases called α, γ and δ. The α-iron, also known as ferrite, is present at temperatures up to $912°C$ and has a BCC phase structure. Between $912°C$ and $1394°C$ the pure iron is known as γ-iron, or austenite, which has an FCC phase structure. Above $1394°C$ and up to the melting point at $1538°C$ the iron is known as δ-iron, or delta ferrite, which also has a BCC phase structure. By adding carbon or other alloying elements the range of the different phases will be altered, for more detailed information see e.g. Krauss (2005). By controlled cooling of the metal, the phases can be prevented from changing, thereby a phase which is present under high temperatures can be obtained at room temperature. However, also new phases such as martensite can be obtained by rapidly cooling austenite.

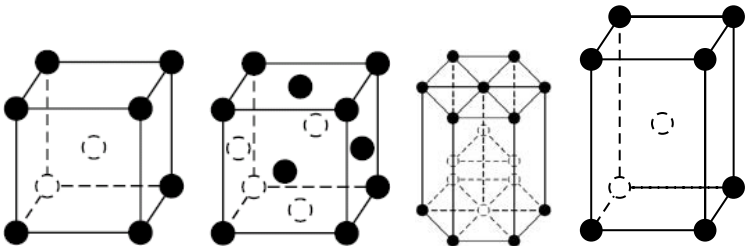

(a) BCC (b) FCC (c) HCP (d) BCT

Figure 1: *Different types of unit cells common for metals, (a) body-centered cubic, (b) face-centered cubic, (c) hexagonal close-packed and (d) body-centered tetragonal.*

2.2 Dual Phase Steel

Dual phase steels mainly consist of ferrite and a minor part of martensitic second phase particles. The second phase particles can be seen as channels and darker areas between the ferritic islands in Figure 2(a). An increase of the amount of hard martensitic particles generally increases strength and reduces ductility. The dual phase is produced either by controlled cooling from the austenitic phase or from the ferrite-austenite phase. The carbon (C) enables the formation of martensite at practical cooling rates. By adding other alloying element such as manganese (Mn),

chromium (Cr), molybdenum (Mo), vanadium (V) and nickel (Ni) individually or in combination, an increase in the hardenability of the steel can be obtained.

2.3 Martensitic Steel

Martensitic steels are produced by a quenching from a temperature in the austenitic range. The steels are characterised by a martensitic matrix with small parts of ferrite or bainite. The martensite can be seen as small needle shaped particles in Figure 2(b). The hardenability can be increased by adding carbon (C) or other alloying elements such as manganese (Mn), silicon (Si), chromium (Cr), molybdenum (Mo), boron (B), vanadium (V) and nickel (Ni).

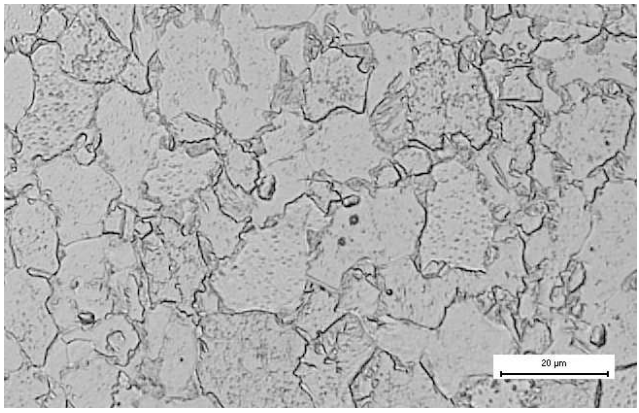

(a)

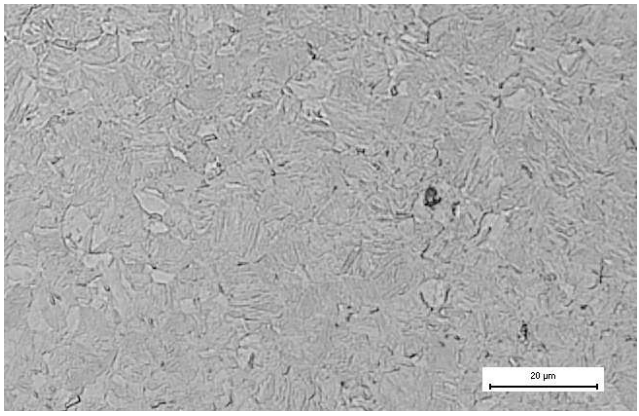

(b)

Figure 2: *Microstructure for: (a) Docol 600DP and (b) Docol 1200M.*

3 Deformation and Fracture

The deformation of steel can be divided into elastic and inelastic parts. The elastic (reversible) deformation, which occurs at the atomic level, does not cause any permanent deformation of the material. Inelastic or plastic deformation, on the other hand, causes permanent deformation. This deformation occurs within the crystal structure by a procedure known as slip. The slip produces crystal defects, called dislocations, and when the deformation continues a large number of these defects occurs. The dislocations in the crystal lattice cause obstacles, which prevent the mobility of subsequent dislocations and thereby contribute to a hardening mechanism. Elastic or plastic deformations do not destroy the atomic arrangement of the material while fractures, on the other hand, cause discontinuities within the material. These discontinuities cause stress concentrations which will increase the 'rate' of fracturing. There are two main types of fracture: brittle and ductile.

Brittle fracture is the breaking of interatomic bonds without noticeable plastic deformation. These fractures occur when the local strain energy becomes larger than the energy necessary to pull the atom layers apart. Brittle fracture occurs mainly in high-strength metals with poor ductility and toughness. However, even metals that have normal ductility may exhibit brittle fracture at low temperatures, in thick sections or at high strain-rates. The surface of a brittle fracture is characterised by its flat appearance and the fracture surface is most often perpendicular to the applied load.

Ductile fracture, on the other hand, is caused by an instability which is the result of very extensive plastic deformations occurring in the surroundings of crystalline defects. The global deformation in a ductile fracture may be either large or small, depending on the density of the defects. The ductile fracture is described as the initiation, growth and coalescence of voids in the material, and finally the loaded area has been reduced and the material fails. The surface of the ductile fracture is characterised by the presence of shear lips, which results in the form of a cup and a cone on the two fracture surfaces. It is also often possible to see the dimples that are caused by the micro-voids. The material examined in this study is assumed to fail only in a ductile manner, and consequently the brittle fracture type is not considered.

In ductile sheet metals or thin walled structures, failure can be caused by one or a combination of the following; (i) ductile fracture, (ii) shear fracture or (iii) instability with localisation, see Figure 3.

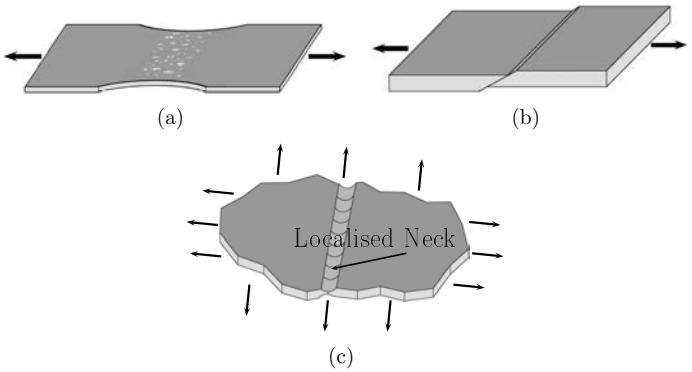

Figure 3: *Failure types in sheet metals, (a) ductile fracture, (b) shear fracture, (c) instability with localisation.*

The ductile fracture arises since most materials contain inclusions or particles, and during deformation voids are likely to nucleate at these locations. Further plastic deformation will cause them to grow until they link together to produce a ductile fracture. Hydrostatic tension will increase the volume of the voids and thereby favours this type of fracture.

Shear fracture can be caused either by extensive slip on the activated slip planes, see Dieter (1986), or as a result of void nucleation in the slip bands. Both of these mechanisms are favoured by shear stresses. When voids nucleate in the slip bands, the loaded area is reduced such that plastic flow localises there. Continued shear increases the area of the voids until separation occurs. Furthermore, as stated by Teirlinck et al. (1988) "Voids which extend in shear need not increase in volume, so shear fracture is less pressure-dependent than ductile fracture, though it remains more pressure-dependent than purely-plastic failure".

Instability or plastic failure occurs if no other mechanism intervenes. In the ordinary tensile test of a sheet metal sample two types of instability can occur: diffuse necking and localised necking. Both mechanisms occur when the strain hardening can no longer compensate for the increased load. Diffuse necking in a tensile test occurs as a reduction of the waist over a length which has about the same size as the width of the waist. Localised necking takes place inside the diffuse zone as a thickness reduction along a narrow band which has about the same size as the thickness. In a more general loading case, localisation can occur without a preceding diffuse necking. Since the strain localises inside the neck the material fails there due to ductile or shear fracture.

4 Constitutive Modelling

In order to be able to formulate the hypothesis on which the constitutive models are based, it is necessary to understand the basic physical deformation mechanisms of the material as described in Chapter 3. Since applications in sheet metal forming and vehicle collision involve large deformations and rotations of the material, it is necessary to formulate the constitutive equations in a consistent manner. By using a co-rotational material framework, see e.g. Belytschko et al. (2000), these large deformations and rotations can be accounted for. The co-rotated Cauchy stress tensor can the be expressed as

$$\hat{\boldsymbol{\sigma}} = \boldsymbol{R}^T \boldsymbol{\sigma} \boldsymbol{R} \tag{1}$$

where $\boldsymbol{R}$ is the orthogonal transformation tensor and $\hat{\boldsymbol{\sigma}}$ denotes the co-rotated Cauchy stress tensor, $\boldsymbol{\sigma}$. From now on $\hat{(\cdot)}$ denotes the co-rotated quantity of $(\cdot)$. The co-rotated rate of deformation tensor is assumed to follow an additive decomposition of the elastic and plastic parts

$$\hat{\boldsymbol{D}} = \hat{\boldsymbol{D}}^e + \hat{\boldsymbol{D}}^p \tag{2}$$

where superscript e and p denotes elastic and plastic parts, respectively. In cases of small elastic deformations, a hypo-elastic stress update can be assumed, i.e.

$$\dot{\hat{\boldsymbol{\sigma}}} = \hat{\boldsymbol{C}} : (\hat{\boldsymbol{D}} - \hat{\boldsymbol{D}}^p) \tag{3}$$

where $\hat{\boldsymbol{C}}$ is the co-rotated fourth order elastic stiffness tensor. Henceforth, the co-rotated superscript, $\hat{(\cdot)}$, will be excluded and all subsequent relations will be related to co-rotated configuration. Plastic deformation will not occur as long as the stress state is considered as elastic. Whether or not the stress state is in the elastic regime is determine by the yield function, f

$$f = \bar{\sigma} - \sigma_{iso}^y \tag{4}$$

where $\bar{\sigma}$ is the effective stress and σ_{iso}^{y} is the current yield stress. The yield function determines the elastic limit of the material and the hypersurface, when $f = 0$ is denoted as the yield surface. As long as $f < 0$ no plastic deformations will occur and when $f = 0$ and $\dot{f} = 0$ plastic flow will occur. The plastic part of the rate of deformation tensor will be determined from the plastic potential, g, according to

$$\boldsymbol{D}^{p} = \dot{\lambda}\frac{\partial g}{\partial \boldsymbol{\sigma}} \tag{5}$$

where $\dot{\lambda}$ is the plastic multiplier and the gradient of g determines in which direction the material will flow. In an associated, in contrast to a non-associated, flow rule the flow is directed normal to the yield surface and in that case the plastic potential and the yield function coincide, i.e. $g = f$. This, assumption has been used throughout this work. Three different modes of loading can occur, (i) elastic case then $\dot{\lambda} = 0$ and $f < 0$, (ii) plastic loading $\dot{\lambda} \geq 0$ and $f = 0$, and (iii) neutral loading if the direction of loading is tangential to the yield surface $\dot{\lambda} = 0$ and $f = 0$. These three cases may be expressed using the Karush-Kuhn-Tucker conditions (KKT-conditions).

$$\dot{\lambda} \geq 0, \quad f \leq 0, \quad \dot{\lambda} f = 0 \tag{6}$$

4.1 Isotropic Hardening

As discussed earlier, plastic deformation is caused by dislocations in the material and the growth of these dislocations will prevent the mobility of new ones and thereby increase the stress that is necessary to produce an increased plastic strain. Most models for describing the current yield stress σ_{iso}^{y} are given as functions of the equivalent plastic strain $\bar{\varepsilon}^{p}$ defined as

$$\bar{\varepsilon}^{p} = \int_{0}^{t} \dot{\bar{\varepsilon}}^{p} \mathrm{d}t \tag{7}$$

where t is the time. However, other quantities, e.g. the plastic strain-rate and temperature, may also affect the hardening of the material. A large amount of analytic functions for describing the hardening can be found in literature. It has also been quite common to use the experimental hardening curves directly. The tensile test is often used for describing hardening up to diffuse necking after which some kind of extrapolation is needed. In this work, an extended Voce law, see Voce (1948), was fitted to the hardening data from the tensile test up to diffuse necking.

After diffused necking an extrapolation using the Hollomon law (see Hollomon (1945)) i.e. a power-law, was adopted by the use of inverse modelling of a shear test. The analytic hardening function can be expressed as

$$\sigma_{iso}^{y}(\bar{\varepsilon}^p) = \begin{cases} \sigma_0 + \sum_{i=1}^{2} Q_{Ri}(1 - e^{-C_{Ri}\bar{\varepsilon}^p}) & \bar{\varepsilon}^p \leq \varepsilon^t \\ A + B(\bar{\varepsilon}^p)^C & \bar{\varepsilon}^p > \varepsilon^t \end{cases} \tag{8}$$

where σ_0, Q_{Ri}, C_{Ri}, A, B and C are material constants and ε^t is the transition point between the extended Voce and Hollomon hardening. The requirements of a smooth curve, i.e. a C^1 transition between the Voce and Hollomon expressions, makes it possible to determine the constants A, B and C with only one new parameter denoted σ'_{100}, which can be interpreted as the stress at 100% plastic strain.

$$\begin{aligned} A + B(\varepsilon^t)^C &= \sigma_0 + \sum_{i=1}^{2} Q_{Ri}(1 - e^{-C_{Ri}\varepsilon^t}) \\ CB(\varepsilon^t)^{C-1} &= \sum_{i=1}^{2} C_{Ri}Q_{Ri}e^{-C_{Ri}\varepsilon^t} \\ A + B &= \sigma'_{100} \end{aligned} \tag{9}$$

The isotropic hardening can be illustrated as an expansion of the yield surface in all directions, see Figure 4(a).

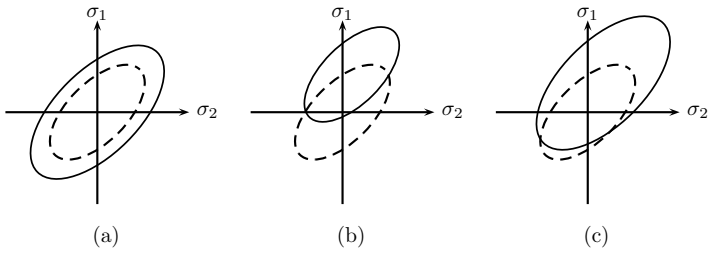

Figure 4: *Different types of hardening (a) isotropic, (b) kinematic and (c) mixed.*

4.2 Kinematic Hardening

Plastic deformation may also introduce anisotropic behaviour of the material, e.g. as manifested by the Bauschinger effect, which is the phenomenon of a lower yield stress in the case of reverse loading. For modelling this effect it is useful to introduce a kinematic hardening model. The kinematic hardening enables the yield surface to move in the stress space, see Figure 4(b), and thereby obtain a reduced yield stress in the case of reverse loading, see Figure 5.

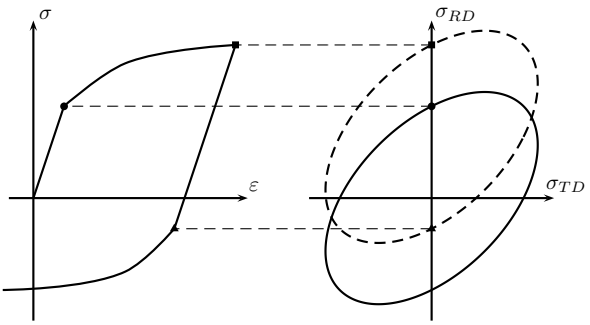

Figure 5: *Ilustraition of the Bauschinger effect in the case of reverse loading.*

The motion of the yield surface is described by the backstress tensor, $\boldsymbol{\alpha}$. The related overstress tensor, $\boldsymbol{\Sigma} = \boldsymbol{\sigma} - \boldsymbol{\alpha}$, replaces the Cauchy stress tensor, $\boldsymbol{\sigma}$, in the effective stress function, $\bar{\sigma} = \bar{\sigma}(\boldsymbol{\sigma} - \boldsymbol{\alpha})$. An interpretation can be seen in Figure 6.

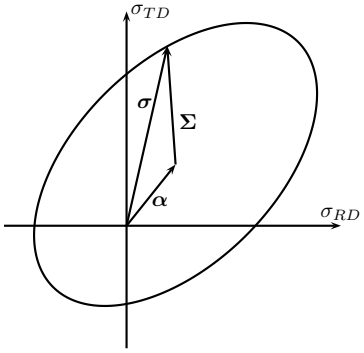

Figure 6: *Interpretation of the overstress,* $\boldsymbol{\Sigma}$*, backstress,* $\boldsymbol{\alpha}$*, and Cauchy stress tensor,* $\boldsymbol{\sigma}$*.*

In this work the evolution of the backstress has been described by a two-component law, presented by Frederick and Armstrong (2007)

$$\dot{\boldsymbol{\alpha}} = \sum_{i=1}^{2} \dot{\boldsymbol{\alpha}}_i = \sum_{i=1}^{2} C_{Xi} \left(Q_{Xi} \frac{\boldsymbol{\Sigma}}{\bar{\sigma}} - \boldsymbol{\alpha}_i \right) \tag{10}$$

where Q_{Xi} and C_{Xi} are material constants determined from pre-strained tensile tests.

4.3 Mixed Hardening

Throughout this work a combination of isotropic and kinematic hardening has been used, i.e. the yield surface can both expand and move, see Figure 4(c). In the special case of uniaxial tension in the ϕ-direction the only non-zero components in the overstress, backstress, and Cauchy stress tensors will be Σ_ϕ, α_ϕ, and σ_ϕ, respectively. The evolution of the backstress can then be expressed as

$$\alpha_\phi(\bar{\varepsilon}^p) = r_\phi \sum_{i=1}^{2} Q_{Xi}(1 - e^{-C_{Xi}\bar{\varepsilon}^p}) \tag{11}$$

where $r_\phi = \Sigma_\phi^y / \bar{\sigma}$ is constant and $\alpha_\phi(0) = 0$ has been used. The yield stress, σ_ϕ^y, can now be expressed as a function of the equivalent plastic strain, $\bar{\varepsilon}^p$.

$$\sigma_\phi^y(\bar{\varepsilon}^p) = r_\phi \begin{cases} \sigma_0 + \sum_{i=1}^{2} \left[Q_{Ri}(1 - e^{-C_{Ri}\bar{\varepsilon}^p}) + Q_{Xi}(1 - e^{-C_{Xi}\bar{\varepsilon}^p}) \right] & \bar{\varepsilon}^p \leq \varepsilon^t \\ A + B(\bar{\varepsilon}^p)^C + \sum_{i=1}^{2} Q_{Xi}(1 - e^{-C_{Xi}\bar{\varepsilon}^p}) & \bar{\varepsilon}^p > \varepsilon^t \end{cases} \tag{12}$$

As can be seen from Equation 12, the mixed hardening may, in the special case of monotonic loading, be interpreted as a summation of isotropic and kinematic hardening, see Figure 7. The total stress at 100% plastic strain, σ_{100}, can now be expressed as the function of the isotropic stress at 100% plastic strain, σ'_{100}, and the saturation of the kinematic hardening.

$$\sigma_{100} = \sigma'_{100} + \sum_{i=1}^{2} Q_{Xi} \tag{13}$$

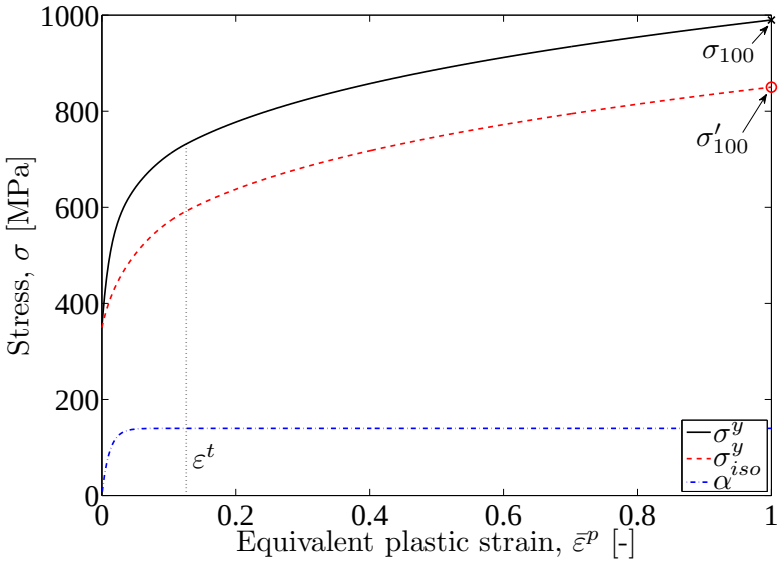

Figure 7: *Hardening decomposition in the case of monotonic loading.*

In order to simplify the parameter identification procedure, a linear mixture between the isotropic and kinematic hardening has been assumed according to

$$\begin{aligned} Q_{Ri} &= (1-\beta_i)Q_i, \quad Q_{Xi} = \beta_i Q_i, \quad i = 1,2 \\ C_{Ri} &= C_{Xi} = C_i, \qquad\qquad\qquad\quad i = 1,2 \end{aligned} \tag{14}$$

where β_i determines the amount of kinematic hardening, and is restricted to a value between 0 and 0.9 in order to avoid infeasible values of C_i.

4.4 Effective Stress

Many expressions for effective stress have been presented over the years. The expression for the effective stress according to von Mises is well known and often used. However, since the von Mises expression only shows isotropic behaviour, and since the rolling process used for producing sheet metals usually leads to different properties in different directions, an anisotropic effective stress function is needed. The rolling direction (RD), transversal direction (TD) and normal direction (ND) are often used to describe the axes of orthotropy. Anisotropy can occur both in the yield stress and in the plastic flow. The anisotropy in plastic flow is described by the Lankford parameter, R, see e.g. Hosford and Cadell (1993), or the plastic strain ratios, k, defined as

$$R_\phi = \frac{\mathrm{d}\varepsilon_T^p}{\mathrm{d}\varepsilon_N^p}, \quad k_\phi = \frac{\mathrm{d}\varepsilon_T^p}{\mathrm{d}\varepsilon_L^p} = \frac{-R_\phi}{R_\phi + 1} \tag{15}$$

where the indices on the logarithmic plastic strain increment indicate the transversal, T, normal N, and longitudinal, L, direction, respectively. The anisotropy in yield stress is described by

$$r_\phi = \frac{\sigma_\phi^y}{\sigma_{ref}} \tag{16}$$

where σ_ϕ^y is the yield stress in the ϕ direction and σ_{ref} is a reference yield stress. Equations 15 and 16 are expressed for the tensile test case but similar equations can be obtained for the balanced biaxial test

$$R_b = k_b = \frac{\mathrm{d}\varepsilon_{TD}^p}{\mathrm{d}\varepsilon_{RD}^p}, \quad r_b = \frac{\sigma_b^y}{\sigma_{ref}} \tag{17}$$

where the subscript b denotes balance biaxial test. The interpretation of the plastic strain ratios, k, and the yield stress ratios, r, are shown in Figure 8.

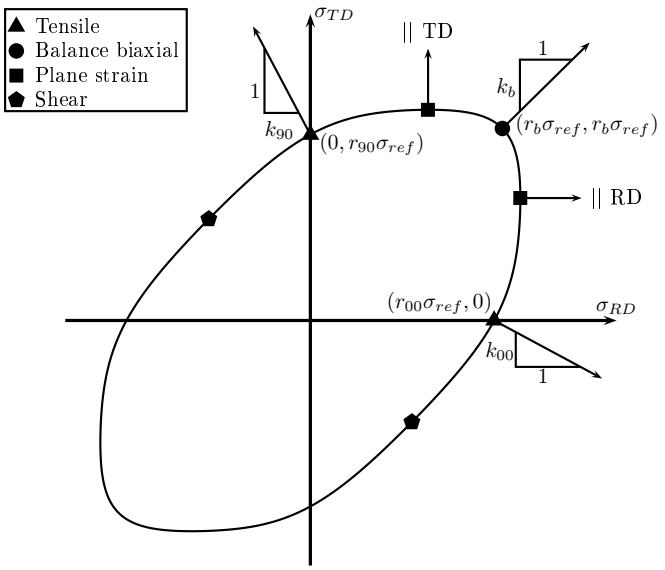

Figure 8: *Yield locus for a plane stress case with* $\tau_{RD} = 0$.

Expressions for representing anisotropic behaviour have been presented by numerous authors and a good overview is given in Banabic et al. (2010). In the present study the model presented by Aretz (2005) has been used

$$\bar{\sigma}(\mathbf{\Sigma}) = \left[\frac{1}{2}\left(|\Delta_1'|^a + |\Delta_2'|^a + |\Delta_1'' - \Delta_2''|^a\right)\right]^{1/a} \tag{18}$$

$$\left.\begin{matrix}\Delta_1' \\ \Delta_2'\end{matrix}\right\} = \frac{A_8\Sigma_{11}^* + A_1\Sigma_{22}^*}{2} \pm \sqrt{\left(\frac{A_2\Sigma_{11}^* - A_3\Sigma_{22}^*}{2}\right)^2 + A_4^2\Sigma_{12}\Sigma_{21}} \tag{19}$$

$$\left.\begin{matrix}\Delta_1'' \\ \Delta_2''\end{matrix}\right\} = \frac{\Sigma_{11}^* + \Sigma_{22}^*}{2} \pm \sqrt{\left(\frac{A_5\Sigma_{11}^* - A_6\Sigma_{22}^*}{2}\right)^2 + A_7^2\Sigma_{12}\Sigma_{21}} \tag{20}$$

where $A_1, ..., A_8$ and a are material constants. The model was originally derived for a plane stress case, where the 11-direction and 22-direction correspond to the RD and TD, respectively. However, a regularisation that enables a C^0 continuous thickness across the element edges has been carried out. Thus the through-thickness normal stress has been included in the effective stress measures, $\Sigma_{11}^* = \Sigma_{11} - \Sigma_{33}$ and $\Sigma_{22}^* = \Sigma_{22} - \Sigma_{33}$, where the 33-direction corresponds to the ND of the sheet. The identification of the parameters has been implemented both by direct methods, using the strain and stress ratios, and inverse modelling of the shear test.

5 Fracture Modelling

Fracture can generally be divided into ductile and brittle fracture, as mentioned in Chapter 3. The ductile fracture is categorised by a considerable amount of plastic deformation prior to material separation. The brittle fracture, on the other hand, occurs at small or no plastic deformation. However, the steels examined in this study are considered as ductile, therefore only this type of fracture will be considered. From a micromechanical point of view the ductile fracture is characterised by nucleation, growth and coalescence of voids in the material until finally the load-bearing area has been reduced and material separation occurs. The reduction in load-bearing area due to voids will lead to material softening. In damage mechanics this effect is described as damage accumulation affecting the constitutive behaviour and the models presented by Gurson (1977) and Lemaitre (1985) are two examples of such models. One simple way to consider this damage is proposed by Lemaitre and Chaboche (1990), given as a relationship between the initial and the damaged area in a certain direction, see Figure 9.

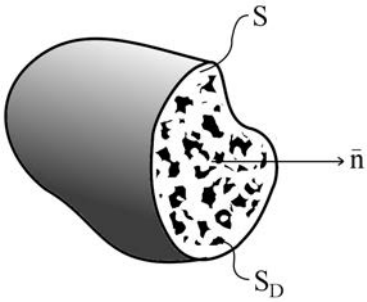

Figure 9: *Initial area, S, and damaged area, S_D, in the normal direction, $\bar{\boldsymbol{n}}$.*

The damage variable, D_n, can then be interpreted as the relationship between the damaged area, S_D, and the initial area, S, respectively.

$$D_n = \frac{S_D}{S} \tag{21}$$

In this definition of damage, ultimate fracture is expected when D_n reaches the value of 1, i.e. when the entire surface is damaged and there is no material left to

keep the parts together. The area that can carry the load on the material is the area given by the difference between the initial and damaged area ($S - S_D$). If the stress far away from the damaged region, σ_∞, is considered and the effective stress working on the material in the damaged region is evaluated, this stress is given by

$$\bar{\sigma} = \frac{S\sigma_\infty}{S - S_D} = \frac{\sigma_\infty}{1 - D_n} \tag{22}$$

Regarding the fracture models, these do not affect the constitutive law before fracture occurs. Most fracture models consider fracture to occur when some state value is reached. Numerous fracture models have been presented and an overview of some of these is presented in Wierzbicki et al. (2005). Several different phenomena may contribute to the failure process. In Teirlinck et al. (1988) four failure phenomena, observed in uniaxial tension specimens, are described: (i) plastic failure, (ii) ductile fracture, (ii) shear fracture and (iv) cleavage and brittle intergranular failure. It should be noted that failure type (iv) cleavage and brittle intergranular failure is considered as a brittle fracture, which is not included in this study. The first three failure types presented are also identified for sheet metals in Hooputra et al. (2004), were the term plastic failure is generalised to represent any sheet instability. Plastic failure or sheet instability is often the primary mechanism leading to failure, even if no material separation occurs at the point of instability. At instability the deformation is localised in a small region and further deformation will rapidly lead to fracture. Failure due to sheet instability is examined separately in Chapter 6. In this chapter the ductile and shear fractures, together with some of the phenomenological models used for their representation in an FE environment, are presented. First some important variables and quantities are specified which are frequently used in the phenomenological models. As stated by Teirlinck et al. (1988) the fracture is strongly connected to hydrostatic pressure, p, which can be expressed in terms of the first invariant of the Cauchy stress, I_1, see Equation 23.

$$\begin{aligned} I_1 &= tr(\boldsymbol{\sigma}) = \sigma_1 + \sigma_2 + \sigma_3 = 3\sigma_m = -3p \\ J_2 &= \frac{1}{2}\boldsymbol{s} : \boldsymbol{s} = \frac{1}{2}tr(\boldsymbol{s}^2) \\ J_3 &= det(\boldsymbol{s}) = \frac{1}{3}tr(\boldsymbol{s}^3) \end{aligned} \tag{23}$$

Another important stress measure is the deviatoric stress tensor, $\boldsymbol{s}$,

$$\boldsymbol{s} = \boldsymbol{\sigma} - \frac{I_1}{3}\boldsymbol{I} \tag{24}$$

where $\boldsymbol{I}$ is the unit tensor. Also the second and third invariants of the deviatoric stress tensor, J_2 and J_3, see Equation 23, are frequently used. From the first

invariants of the Cauchy stress, I_1, the second and third invariants of the deviatoric stress, J_2 and J_3, the Haigh-Westergaard coordinates, ξ, ρ and θ can be defined

$$\begin{aligned} \xi &= \frac{1}{\sqrt{3}} I_1 \\ \rho &= \sqrt{2J_2} = \sigma_{vM} \\ cos(3\theta) &= \frac{\sqrt{27}}{3} \frac{J_3}{J_2^{3/2}} \end{aligned} \tag{25}$$

where σ_{vM} is the equivalent von Mises stress. These coordinates can be explained from Figure 10, where the ξ-axis is aligned with the hydrostatic axis ($\sigma_1 = \sigma_2 = \sigma_3$), ρ-axis is the radius of the von Mises cylinder and θ is the Lode angle, cf. also Figure 11. The point B in the principal stress space can now be defined in the Haigh-Westergaard coordinates as

$$\begin{bmatrix} \sigma_1 \\ \sigma_2 \\ \sigma_3 \end{bmatrix} = \frac{\xi}{\sqrt{3}} \begin{bmatrix} 1 \\ 1 \\ 1 \end{bmatrix} + \sqrt{\frac{2}{3}} \rho \begin{bmatrix} cos(\theta) \\ cos(\theta - 2\pi/3) \\ cos(\theta + 2\pi/3) \end{bmatrix} \tag{26}$$

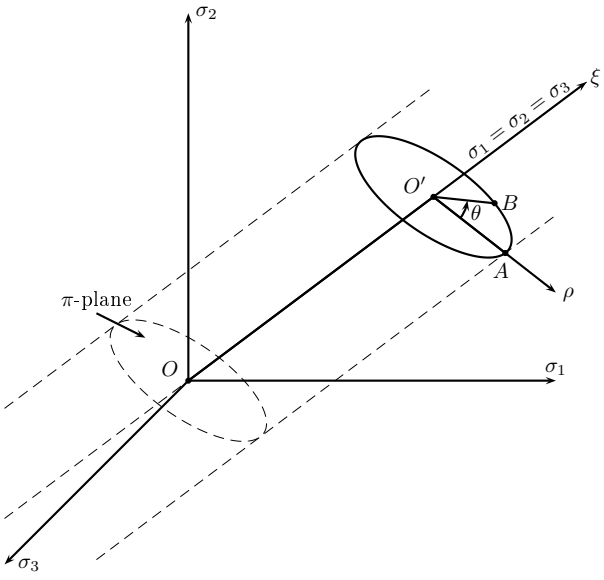

Figure 10: *Von Mises cylinder shown in the principal Cauchy stress space.*

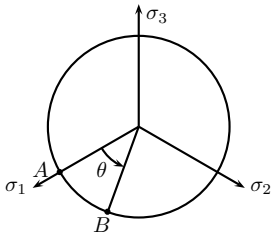

Figure 11: *Von Mises cylinder shown in the π-plane.*

The importance of the Lode angle, θ, on fracture has been reported, e.g. by Bai and Wierzbicki (2008). Also the importance of the stress triaxiality, η, which is the relationship between hydrostatic pressure and the equivalent von Mises stress, see Equation 27, has been demonstrated by several authors e.g. Oyane et al. (1980) and Bao and Wierzbicki (2004).

$$\eta = -\frac{p}{\sigma_{vM}} \tag{27}$$

5.1 Ductile Fracture

Even if the fracture models do not affect the elasto-plastic or elasto-viscoplastic constitutive laws and thus produce a material softening, it is useful to consider them as a type of growing function. One useful representation is

$$\int_0^{\varepsilon_f} F(\text{state variables}) \mathrm{d}\bar{\varepsilon}^p \leq C \tag{28}$$

where the function, F, may depend on any state variable and is integrated on the effective plastic strain, $\bar{\varepsilon}^p$. The state variables can be divided into observable variables, e.g. temperature, T, total strain, ε, or internal, e.g. plastic strain, $\boldsymbol{\varepsilon}^p$, or stress state, $\boldsymbol{\sigma}$, among others. The simplest form of Equation 28 is when $F \equiv 1$, in which case the model predicts the equivalent plastic strain to fracture. However, a fracture criterion given by constant equivalent plastic strain to fracture is contrary to experimental observations.

5.2 Shear Fracture

Shear fracture is a result of extensive slip on the activated slip planes. Consequently this fracture is favoured by shear stresses. The shear fracture can also be found under certain conditions when voids nucleate in the slip band and reduce the load-bearing area, so that continuous plastic flow localises there. Since sheet metal applications often are modelled by shell elements, which most often are restricted to plane stress assumptions, it is necessary to construct a fracture model that can predict fracture due to transversal shear.

5.3 Phenomenological Fracture Models

A short review of some of the phenomenological fracture models presented in literature is given below.

The Cockroft and Latham Criterion

Cockroft and Latham (1968) suggested a criterion based on an accumulated stress and plastic strain. More precisely they argued that the plastic work must be an important factor for the fracture. The total amount of plastic work done per unit volume at the fracture point is

$$W^p = \int_0^{\varepsilon_f} \bar{\sigma} \mathrm{d}\bar{\varepsilon}^p \tag{29}$$

where $\bar{\sigma}$ is the current equivalent stress ($\bar{\sigma} = \sigma^y_{iso}$), ε_f is the fracture strain, and $\bar{\varepsilon}^p$ the equivalent plastic strain. However, the current stress $\bar{\sigma}$, unlike the peak stress σ_1, is not influenced by the shape of the necked region. A criterion based on the total amount of plastic work will therefore predict a fracture independent of this shape, which is contrary to experiments. Therefore, the total amount of plastic work cannot provide a good criterion by itself, since necking is important according to experimental observations. A more reasonable fracture criterion would be to take the magnitude of the highest tensile stress into account. Therefore, Cockroft and Latham proposed that fracture occurs in a ductile material when

$$W = \int_0^{\varepsilon_f} \bar{\sigma} \left(\frac{< \sigma_1 >}{\bar{\sigma}} \right) \mathrm{d}\bar{\varepsilon}^p \tag{30}$$

reaches a critical value, W_c, for a given temperature and strain rate. The non-dimensional stress concentration factor, $\left(\frac{<\sigma_1>}{\bar{\sigma}}\right)$, represents the effect of the highest tensile stress, $<\sigma_1>=max(\sigma_1,0)$. The reduced form

$$W = \int_0^{\varepsilon_f} <\sigma_1> \mathrm{d}\bar{\varepsilon}^p \leq W_c \tag{31}$$

is used for the fracture evaluation, and fracture is expected when the integral reaches a critical value, W_c, which is determined from experiments. The Cockroft and Latham model implies that fracture in a ductile material depends both on the stresses and plastic strain states, i.e. neither stress nor strain alone can describe ductile fracture. The benefit of using the largest principal stress, σ_1, is that it can be expressed as a function of the hydrostatic pressure, p, the second invariant of the deviator stress, J_2 and the Lode angle, θ, as

$$\sigma_1 = -p + \sqrt{\frac{4J_2}{3}}\cos\theta \tag{32}$$

The Wilkins Criterion

The model by Wilkins et al. (1980), also known as the R_cD_c model, states that two factors increase the fracture threshold: the hydrostatic stress and the asymmetric stress. The hydrostatic stress accounts for the growth of holes by spalling. Interrupted tension tests have shown initiation and growth of voids which form a fracture surface. The asymmetric stress accounts for the observation that the elongation at fracture decreases as the shear load increases in fracture tests with combined stress loads. The accumulated damage is expressed as

$$D = \int_0^{\varepsilon_f} \omega_1\,\omega_2\,\mathrm{d}\bar{\varepsilon}^p \leq 1 \tag{33}$$

and the weight factors for the hydrostatic stress and the asymmetric stress are expressed as

$$\omega_1 = \left(\frac{1}{1-C_3\sigma_m}\right)^{C_1}, \quad \omega_2 = (2-A_D)^{C_2} \tag{34}$$

where ω_1 is the hydrostatic pressure weight, ω_2 is the asymmetric stress weight, $\mathrm{d}\bar{\varepsilon}^p$ is the equivalent plastic strain increment, σ_m is the hydrostatic pressure and C_1, C_2, and C_3 are material constants. The parameter A_D included in the asymmetric stress weight, ω_2 is defined as

$$A_D = \min\left(\left|\frac{s_2}{s_3}\right|, \left|\frac{s_2}{s_1}\right|\right) \tag{35}$$

where s_1, s_2 and s_3 are the principal stress deviators. The parameter A_D ranges from 0 to 1, and when $A_D = 1$ the stress field is symmetric (and asymmetric when $A_D = 0$). Fracture is expected when the damage parameter, D, in Equation 33 reaches 1.

The Oyane Criterion

Oyane et al. (1980) suggested a fracture model to consider the effect of stress triaxiality on ductile fracture. The model is derived from the plasticity theory for porous media as

$$\int_0^{\varepsilon_f} (C_1 + \eta)\, \mathrm{d}\bar{\varepsilon}^p \leq C_2 \tag{36}$$

where C_1 and C_2 are material constants and η is the stress triaxiality.

The Johnson and Cook Criterion

The fracture model presented by Johnson and Cook (1985) is a purely phenomenological model, which is based on a similar relation as the hardening model presented by Johnson and Cook (1983). The model uses a damage parameter D, and when this parameter reaches the value of 1, ultimate fracture is expected. The definition of the damage parameter is

$$D = \int_0^{\varepsilon_f} \frac{1}{\Phi} \mathrm{d}\bar{\varepsilon}^p \leq 1 \tag{37}$$

where ε_f is the equivalent strain to fracture and $d\bar{\varepsilon}^p$ is the increment of equivalent plastic strain. The expression for the function Φ is given as

$$\Phi = \left(C_1 + C_2 e^{-C_3 \eta}\right)\left[1 + C_4 \ln\left(\frac{\dot{\bar{\varepsilon}}^p}{\dot{\varepsilon}_0}\right)\right](1 + C_5 T) \tag{38}$$

where $C_1, ..., C_5$ are material constants, which can be determined from experiments, η is the stress triaxiality, $\dot{\bar{\varepsilon}}^p$ is the equivalent plastic strain-rate, $\dot{\varepsilon}_0$ is a reference strain-rate and T is the temperature. As noted from the Equations 37 and 38 the model depends on strain, strain-rate, temperature and stress triaxiality.

The Bressan and Williams Criterion

Shell elements are often used for modelling sheet metal applications, but are frequently restricted to plane stress conditions. Thus, they are not able to describe transversal shear stresses. It is therefore necessary to consider a fracture criterion which can be used to predict this phenomenon. Bressan and Williams (1983) suggested a model for predicting instability through the thickness of a sheet metal. They suggested that the plastic strain increment should be equal to zero at an inclined direction through the thickness of the sheet, i.e. $\mathrm{d}\varepsilon_t^p = 0$ in the $\boldsymbol{e}_t$-direction shown in Figure 12. By assuming that the directions of the principal stress and strains coincide, and by using the stress and strain tensor components according to Equation 39, together with the rotation tensor to rotate the stress and strains to the incline directions $(\boldsymbol{e}_n, \boldsymbol{e}_2, \boldsymbol{e}_t)$,

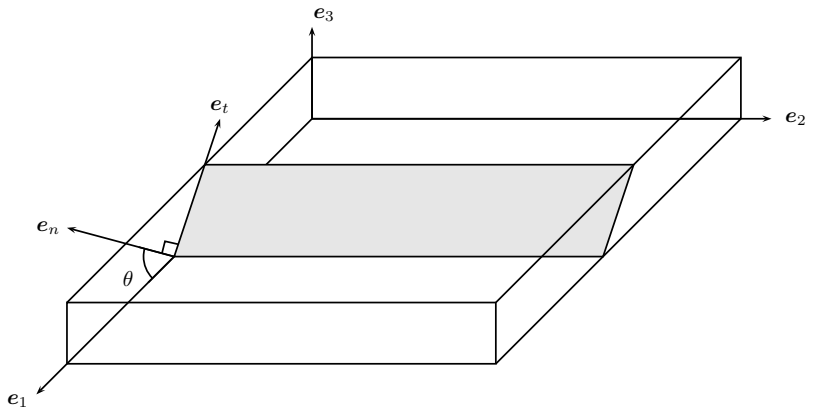

Figure 12: *Inclined plane through the thickness of the sheet. The stress and strain on the $\boldsymbol{e}_t$-plane is determined from the values in the coordinate axis $\boldsymbol{e}_i$, where $i = 1...3$, and the angle, θ.*

$$\boldsymbol{\sigma} = \begin{bmatrix} \sigma_1 & 0 & 0 \\ 0 & \sigma_2 & 0 \\ 0 & 0 & 0 \end{bmatrix}, \qquad \mathrm{d}\boldsymbol{\varepsilon^p} = \begin{bmatrix} \mathrm{d}\varepsilon_1^p & 0 & 0 \\ 0 & \mathrm{d}\varepsilon_2^p & 0 \\ 0 & 0 & \mathrm{d}\varepsilon_3^p \end{bmatrix} \tag{39}$$

the strain increment in the $\boldsymbol{e}_t$-direction and the shear stress on the inclined surface can be found as

$$\mathrm{d}\varepsilon_t^p = \sin^2\theta \mathrm{d}\varepsilon_1^p + \cos^2\theta \mathrm{d}\varepsilon_3^p = 0 \tag{40}$$

and

$$\sigma_{tn} = -(\sigma_1)\sin\theta\cos\theta \tag{41}$$

Assuming that fracture occurs when the shear stress, σ_{tn}, on the inclined surface reach a critical value τ_c, and that the material is plastically incompressible, the following is obtained

$$\cos 2\theta = \frac{-\mathrm{d}\varepsilon_2^p}{2\mathrm{d}\varepsilon_1^p + \mathrm{d}\varepsilon_2^p} = \frac{-\beta}{2+\beta} \tag{42}$$

and

$$\sin 2\theta = -\frac{2\tau_c}{\sigma_1} \tag{43}$$

Here $\beta = \mathrm{d}\varepsilon_2^p/\mathrm{d}\varepsilon_1^p$ is the relationship between the in-plane principal plastic strains and τ_c is a material constant. From Equations 42 and 43 the following inequality can be obtained

$$\tau = \frac{\sigma_1}{2}\sqrt{1 - \left(\frac{-\beta}{2+\beta}\right)^2} \leq \tau_c \tag{44}$$

where $\sigma_1/2$ is the shear stress on the inclined surface, cf. Figure 12. As long as the inequality is fulfilled no fracture is expected due to through-thickness shear. However, in this work a normal stress through the thickness has been introduced to obtain C^0 continuity over the element edges. Therefore, the criterion in Equation 44 is modified such that

$$\tau = \frac{\sigma_1 - \sigma_{ND}}{2}\sqrt{1 - \left(\frac{-\beta}{2+\beta}\right)^2} \leq \tau_c \tag{45}$$

where σ_{ND} is the through-thickness normal stress, and thus $(\sigma_1 - \sigma_{ND})/2$ is the shear stress on the inclined surface.

The Han and Kim Criterion

Han and Kim (2003) suggested a criterion for ductile fracture, which combines the model by Cockcroft-Latham with a maximum shear stress criterion and the through thickness strain. Thus,

$$\int_0^{\varepsilon_f} < \sigma_1 > \mathrm{d}\bar{\varepsilon}^p + C_1(\sigma_1 - \sigma_3)/2 + C_2\varepsilon_t \leq C_3 \tag{46}$$

where C_1, C_2, and C_3 are material parameters, determined from experiments, and ε_t is the thickness strain. Here it has been used so that the principal stresses follows $\sigma_1 > \sigma_2 > \sigma_3$. Then the term $(\sigma_1 - \sigma_3)/2$ is the maximum shear stress.

6 Modelling Instability

Even if there is no material separation during an instability, it is most often considered as a limit of the operational use of the product. At instability the deformation is localised as a narrow band of the same width as the thickness of the sheet, see e.g. Dieter (1986). Due to the localisation, further deformation will rapidly lead to a material fracture. The prediction of instability limits is therefore important in order to find the correct failure behaviour.

6.1 Instability in Plane Strain

The instability limit can, for the special case of plane strain, be derived analytically. However, the elastic strains are neglected here and all strains are assumed to be plastic. Consider a rod with a length, l, width, w, and thickness, t. The force in the length direction can be expressed as $F_{11} = \sigma_{11} wt$, where the subscript 11 corresponds to the length direction. The instability arises when the force reaches a maximum viz. $\mathrm{d}F_{11} = 0$. In terms of stress and strains, the following is obtained

$$\frac{\mathrm{d}\sigma_{11}}{\mathrm{d}\varepsilon^p_{11}} = \sigma_{11} \tag{47}$$

where $\frac{\mathrm{d}l}{l} = \mathrm{d}\varepsilon^p_{11}$, $\frac{\mathrm{d}w}{w} = \mathrm{d}\varepsilon^p_{22} = 0$ (plane strain), $\frac{\mathrm{d}t}{t} = \mathrm{d}\varepsilon^p_{33}$, has been used and the fact that the material is assumed to be plastically incompressible, i.e. $\mathrm{d}\varepsilon^p_{11} + \mathrm{d}\varepsilon^p_{22} + \mathrm{d}\varepsilon^p_{33} = 0$. By assuming a plane stress assumption, the stress and strain components can be expressed as

$$\boldsymbol{\varepsilon} = \varepsilon^p_{11} \begin{bmatrix} 1 & 0 & 0 \\ 0 & 0 & 0 \\ 0 & 0 & -1 \end{bmatrix}, \quad \boldsymbol{\sigma} = \sigma_{11} \begin{bmatrix} 1 & 0 & 0 \\ 0 & \gamma & 0 \\ 0 & 0 & 0 \end{bmatrix} \tag{48}$$

where γ is the stress ratio producing plane strain deformation, see Figure 13.

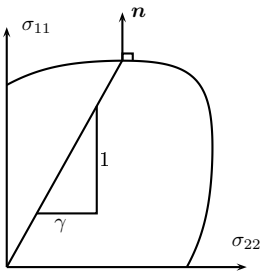

Figure 13: *Stress path for a plane strain condition.*

By using the principle of equivalent plastic work,

$$\boldsymbol{\sigma} : \boldsymbol{\varepsilon}^p = \sigma_{11}\varepsilon_{11}^p = \bar{\sigma}\bar{\varepsilon}^p \tag{49}$$

where $\bar{\sigma}$ and $\bar{\varepsilon}^p$ are the effective stress and plastic strain, respectively. Since the effective stress, $\bar{\sigma}$, is a homogeneous function of degree one, i.e. $\bar{\sigma}(\chi\boldsymbol{\sigma}) = |\chi|\bar{\sigma}(\boldsymbol{\sigma})$, the stress in the 11-direction can be expressed as

$$\sigma_{11} = \overbrace{\frac{1}{\bar{\sigma}(\sigma_{11}=1, \sigma_{22}=\gamma, \sigma_{12}=0)}}^{p(\gamma)}\bar{\sigma} \tag{50}$$

From Equation 49 the strain can be expressed as

$$\varepsilon_{11} = \frac{1}{p(\gamma)}\bar{\varepsilon}^p \tag{51}$$

From the yield function $\bar{\sigma} = \sigma_{iso}^y(\bar{\varepsilon}^p)$ is known. Therefore, the instability condition, Equation 47, can be expressed in terms of the yield stress, σ_{iso}^y, where the only unknown is the equivalent strain, $\bar{\varepsilon}^p$.

$$\frac{\mathrm{d}\sigma_{iso}^y(\bar{\varepsilon}^p)}{\mathrm{d}\bar{\varepsilon}^p} = \frac{1}{p(\gamma)}\sigma_{iso}^y(\bar{\varepsilon}^p) \tag{52}$$

The strains causing localisation can then be evaluated from Equation 51. The instability at plane strain is therefore strongly affected by the hardening after necking, and by increasing σ_{100} from Equation 13 the strain at instability can be increased, see Figure 14.

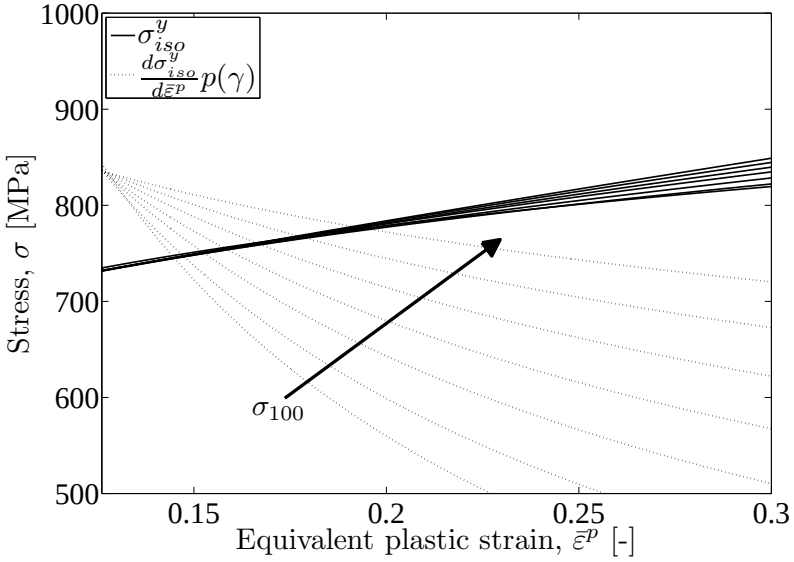

Figure 14: *Instability under plane strain.*

6.2 Analytical Instability Models

The theory in Section 6.1 can be used to obtain similar expressions for more general instability models. In Aretz (2004) a strategy is given for the computational implementation of the models according to Hill (1952), Swift (1952) and Hora et al. (1996). These models are presented in terms of principal stresses and strains, see Table 2. Some general assumptions for all these models are

- Elastic strains are neglected, i.e. $\varepsilon = \varepsilon^p$ and $\mathrm{d}\varepsilon = \mathrm{d}\varepsilon^p$.
- Plane stress is assumed, i.e. σ_{11}, σ_{22} are the only non-zero principal stresses ($\sigma_{11} \geq \sigma_{22}$).
- No shear strains are assumed, i.e. ε^p_{11}, ε^p_{22} and ε^p_{33} are the only non-zero strains. ε^p_{11} and ε^p_{22} are the major and minor principal strains, respectively.
- The material is assumed to be plastically incompressible, i.e. $\mathrm{d}\varepsilon^p_{11} + \mathrm{d}\varepsilon^p_{22} + \mathrm{d}\varepsilon^p_{33} = 0$.
- Linear strain paths are assumed, i.e. $\varepsilon^p_{11}/\varepsilon^p_{22} = \mathrm{d}\varepsilon^p_{11}/\mathrm{d}\varepsilon^p_{22} = const.$
- Only isotropic hardening is considered and the material follows an associative flow rule.
- The anisotropy axes coincide with the principal strain and stress axes.

Table 2: *Instability models according to Hill (1952), Swift (1952) and Hora et al. (1996) expressed in terms of principal stresses and strains.*

Hill	$\dfrac{\mathrm{d}\sigma_{11}}{\mathrm{d}\varepsilon^p_{11}} = \sigma_{11}(1-\beta) \qquad \beta = \dfrac{\mathrm{d}\varepsilon^p_{22}}{\mathrm{d}\varepsilon^p_{11}}$
Swift	$\dfrac{\mathrm{d}\sigma_{11}}{\mathrm{d}\varepsilon^p_{11}} = \sigma_{11}$
Hora et al.	$\dfrac{\partial\sigma_{11}}{\partial\varepsilon^p_{11}} + \dfrac{\partial\sigma_{11}}{\partial\beta}\dfrac{\partial\beta}{\partial\varepsilon^p_{11}} = \sigma_{11} \quad \beta = \dfrac{\mathrm{d}\varepsilon^p_{22}}{\mathrm{d}\varepsilon^p_{11}}$

The stress and strain-rate ratios are expressed by γ and β, respectively. However, the strain-rate ratio can be expressed in terms the stress ratio, γ, since an associative flow rule is assumed.

$$\beta = \frac{\mathrm{d}\varepsilon^p_{22}}{\mathrm{d}\varepsilon^p_{11}} = \left.\frac{\partial\bar{\sigma}/\partial\sigma_{22}}{\partial\bar{\sigma}/\partial\sigma_{11}}\right|_{\sigma_{11}=1,\sigma_{22}=\gamma} \tag{53}$$

Thus, the strain-rate ratio can be expressed as $\beta = \beta(\gamma)$. From Equation 50 the stress can be expressed in terms of the equivalent measurement and the positive function $p(\gamma)$. The equivalence of principle plastic work can now be used to express the strain in terms of the equivalent strain measurement

$$\bar{\sigma}\bar{\varepsilon}^p = \sigma_{11}\varepsilon^p_{11} + \sigma_{22}\varepsilon^p_{22} = \sigma_{11}\varepsilon^p_{11}(1+\gamma\beta(\gamma)) \quad \Rightarrow \quad \varepsilon^p_{11} = \frac{1}{q(\gamma)}\bar{\varepsilon}^p \tag{54}$$

where the function $q(\gamma) = p(\gamma)(1+\gamma\beta(\gamma))$ has been introduced. By prescribing the yield stress, $\sigma^y_{iso} = Y$, as a function of the accumulated equivalent plastic strain, $\bar{\varepsilon}^p$, the localisation criteria can be expressed as shown in Table 3.

Table 3: *Instability models according to Hill (1952), Swift (1952) and Hora et al. (1996) expressed in terms of yield stress functions.*

Hill	$Y'(\bar{\varepsilon}^p)q(\gamma) = Y(\bar{\varepsilon}^p)(1+\beta(\gamma))$
Swift	$Y'(\bar{\varepsilon}^p)q(\gamma) = Y(\bar{\varepsilon}^p)$
Hora et al.	$Y'(\bar{\varepsilon}^p)p(\gamma)q(\gamma) - Y(\bar{\varepsilon}^p)\dfrac{p(\gamma)q(\gamma)\beta(\gamma)}{\beta'(\gamma)\bar{\varepsilon}^p} = p(\gamma)Y(\bar{\varepsilon}^p)$

In Table 3 new derivatives have been introduced defined as $Y'(\bar{\varepsilon}^p) = \mathrm{d}Y(\bar{\varepsilon}^p)/\mathrm{d}\bar{\varepsilon}^p$, $\beta'(\gamma) = \mathrm{d}\beta(\gamma)/\mathrm{d}\gamma$ and $p'(\gamma) = \mathrm{d}p(\gamma)/\mathrm{d}\gamma$. From these equations the only unknown

quantity is the accumulated equivalent plastic strain, $\bar{\varepsilon}^p$, if the stress path is assumed to be prescribed and proportional. By prescribing different strain paths (i.e. stress ratios) a FLC can be constructed.

6.3 The Marciniak and Kuczynski Model

The model described by Marciniak and Kuczynski (1967), often referred to as the MK model, considers an imperfection or defect in a sheet metal, most often realised as a thickness reduction over a narrow band, see Figure 15. The thickness difference is described by an imperfection factor $F = t_B/t_A$.

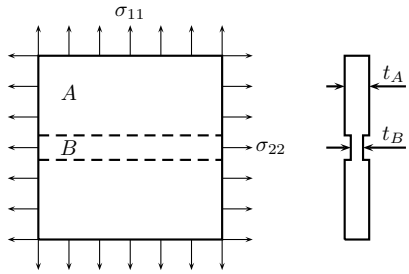

Figure 15: *The geometry for the MK-model.*

The elastic deformations are neglected in this analysis. Due to equilibrium in the region B the stress in the imperfection can be expressed as

$$\sigma_{11}^B = \frac{t_A}{t_B}\sigma_{11}^A = \frac{\sigma_{11}^A}{F} \tag{55}$$

Compatibility in the 22-direction requires that the strains in this direction must be identical in both the regions

$$\varepsilon_{22}^A = \varepsilon_{22}^B \;\Leftrightarrow\; \mathrm{d}\varepsilon_{22}^A = \mathrm{d}\varepsilon_{22}^B \tag{56}$$

A plane stress state is used and the material is considered as plastically incompressible. Furthermore, a proportional deformation of the region A is specified as

$$\boldsymbol{\sigma}^A = \sigma_{11}^A \begin{bmatrix} 1 & 0 & 0 \\ 0 & \gamma_A & 0 \\ 0 & 0 & 0 \end{bmatrix}, \quad \boldsymbol{\varepsilon}^A = \varepsilon_{11}^A \begin{bmatrix} 1 & 0 & 0 \\ 0 & \beta_A & 0 \\ 0 & 0 & -(1+\beta_A) \end{bmatrix} \tag{57}$$

where γ_A and β_A describe the deformation. The strain ratio, β_A, can be expressed as,

$$\beta_A = \left. \frac{\partial \bar{\sigma} / \partial \sigma_{22}}{\partial \bar{\sigma} / \partial \sigma_{11}} \right|_{\sigma_{11}=1, \sigma_{22}=\gamma_A, \sigma_{12}=0} \tag{58}$$

since that the material is assumed to follow an associated flow rule. The stress σ_{11}^B can then be found from Equation 55. Since the stress in the length direction is slightly larger inside the band, the yield surface is first reached here. However, due to the compatibility condition, Equation 56, no plastic deformation can occur before the yield surface is also reached for region A. If further deformation occurs, the state of stress in the band is moved on the yield surface towards point B_1, see Figure 16(a). At a certain point the yield limit is also reached in the uniform region, point A_1, and plastic deformation can occur. However, due to the restriction that the strain in the 22-direction needs to be equal in both regions A and B, the equivalent plastic strain will be different, i.e. $\bar{\varepsilon}_B^p > \bar{\varepsilon}_A^p$, see Figure 16(b). A continuous deformation will increase the difference in equivalent plastic strain and move the stress state in region B towards the state of plane strain, see B_f in Figure 16(a). When the state of plane strain is reached, instability is assumed to occur.

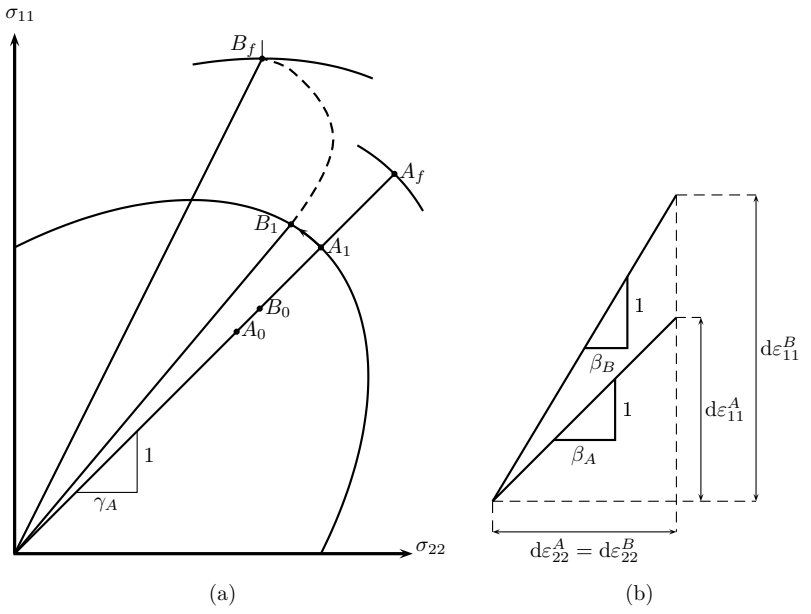

Figure 16: *MK model (a) stress state for region A and B and (b) relationship between the strain paths.*

6.4 Finite Element Model

Detailed FE models can generally be used to capture the instability phenomena, e.g. Lademo et al. (2004a). To predict the instability, a square patch of elements, see Figure 17, is used with has an inhomogeneity in its thickness distribution. The patch is stretched in different directions to obtain linear strain paths and to produce the FLC in the forming limit diagram (FLD). The strain paths have been prescribed such that

$$\delta_{11} = w_0 \left(e^{\varepsilon cos\theta} - 1\right), \quad \delta_{22} = w_0 \left(e^{\varepsilon sin\theta} - 1\right) \tag{59}$$

where w_0 is the width of the plate, $\theta = tan\beta$ is the relationship between the strains, and ε has been given as a smooth function of time.

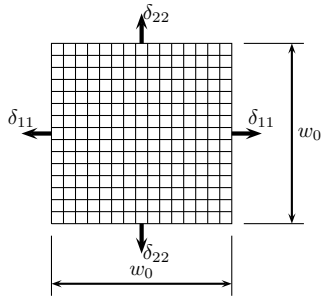

Figure 17: *Patch of elements for the instability prediction.*

The focus of the study is on the relationship between the local thickness strain increment and the average thickness strain increment, on an area Ω.

$$\zeta_i = \frac{\Delta\varepsilon_{33,i}}{\Delta\varepsilon_{33}^{\Omega}} \tag{60}$$

The average thickness strain increment is

$$\Delta\varepsilon_{33}^{\Omega} = \frac{1}{N}\sum_{i=1}^{N}\Delta\varepsilon_{33,i} \tag{61}$$

where N is the number of elements in the domain Ω. Instability is assumed to occur when ζ_i reaches a critical value in any element i. However, since the strain-rate shows an oscillating behaviour pattern, it is necessary to define the point of

instability over a period of time, viz. ζ_i needs to exceed a critical value ζ_c for a number of time steps n_t. Lademo et al. (2004a) describe the thickness variation as a normal distributed random field with mean value μ and standard deviation, usually denoted σ. However, according to Fyllingen et al. (2009) one drawback with this method is that the variation depends on the number of nodes. Hence, a refinement of the FE mesh will lead to a different random field. Consequently the variation in the thickness is described here independently of the FE mesh

$$t(x, y) = \mu(x, y) + Z(x, y) \tag{62}$$

where both the mean value, μ, and the residual term, Z, may depend on the global coordinates x and y. In this work the mean value has been set to a constant value, i.e. $\mu(x, y) = \mu$, and for the residual term, Z, a Gaussian zero mean homogeneous random field according to Shinozuka and Deodatis (1996) has been used.

6.5 Evaluation of Instability

The different methods presented above can be summarized in an FLD, see Figure 18. As can be seen all models predict about the same instability limit in their domain of usage. However, all instability models used here, except the FE-based model which can be used for any material model, use a plane stress assumption. The material model presented in Chapter 4 is modified to also include a through-thickness normal stress, σ_{ND}, to obtain a C^0 continuous element formulation. Therefore, the FE-based model has been used throughout this study for instability predictions. A square patch of finite elements is used with an inhomogeneous thickness distribution in order to predict the instability. The patch is stretched such that linear strain paths are obtained in different directions. In Lademo et al. (2004a) and Lademo et al. (2004b) the limit strains causing localisation are considered as the total strains in the patch when an instability has occurred. However, in this study the local strains in an element within the localisation area are considered. In order to find the strain limit at localised necking in the patch, two elements are considered: one inside the localisation zone and one some distance away from it, see Figure 19(a) elements A and B, respectively. The limit value is then obtained as the strains in the finite element within the localisation zone at a stage when the strains in the distant element do not increase, see Figure 19(b).

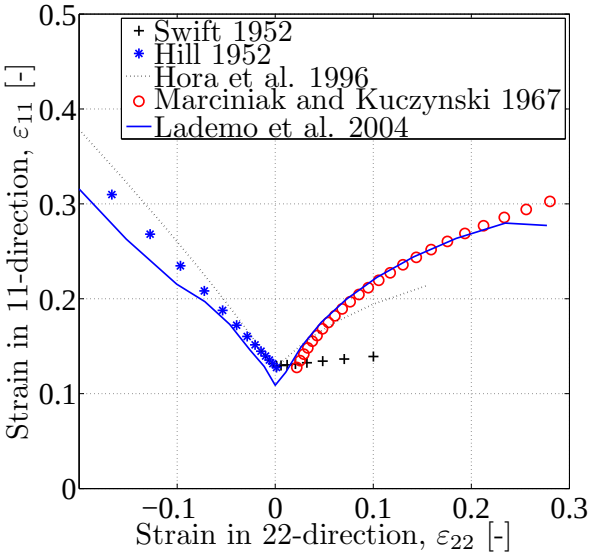

Figure 18: *Different models to predict instability.*

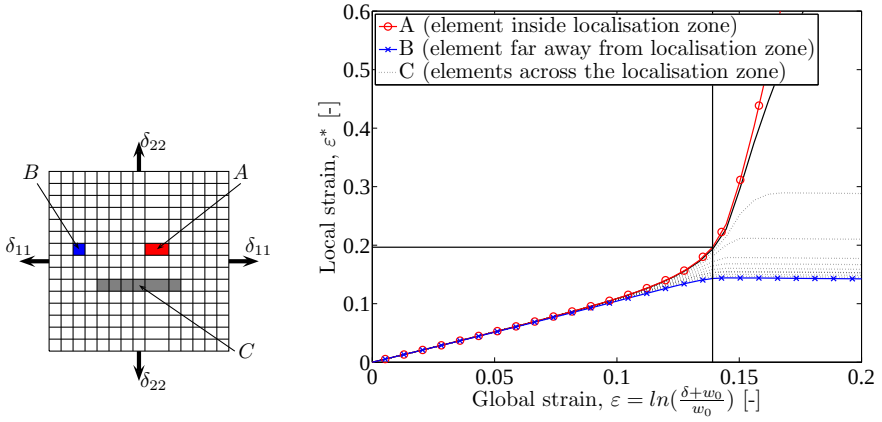

(a) (b)

Figure 19: *Evaluation procedure for instability limits, (a) chosen elements and (b) local vs. global strain.*

7 Mechanical Experiments

A number of mechanical tests have been performed to calibrate both the constitutive relations and the fracture models. In this study six different mechanical tests have been conducted:

- Pre-deformation
- Tensile
- Shear
- Plane strain
- Bulge
- Nakajima

The pre-deformation specimens have been performed in an MTS hydraulic machine with a 250 kN load cell. The tensile, shear and plane strain tests have been carried out in an INSTRON 5582 machine with a 10 kN load cell.

7.1 Pre-Deformation

Pre-deformation of large specimens, according to Figure 20(a), was performed in order to produce broken strain paths. Due to limitations of the test rig, the specimen length, width and thickness were 1100 mm, 125 mm and 1.5 mm, respectively. Since all material tests in this work were performed under quasi-static conditions the deformation was performed at a constant crosshead speed of 5 mm/min, which resulted in a strain-rate of approximately 10^{-4} s^{-1}. The unloading was set to last for 1 min. The design of the specimen was made in an attempt to maximize the zone of homogenous strain. The homogeneity at the centre of the specimen was confirmed both by FE simulation, see Figure 20(b), and by ocular measurements. The mid section of the specimen was divided into 16 equal sections, in which the thickness, width and length were measured both before and after completed loading. The pre-deformations were performed both in the RD and in the TD, i.e. $\psi = 0°$ and $\psi = 90°$ according to Figure 21. For each direction the materials have been pre-deformed to two significant strain levels; one level chosen close to the strain causing diffused necking and the other level chosen to approximately half of

the first one. The levels of pre-straining for each material and direction are displayed in Table 4. After the pre-straining operation tensile, shear and plane strain specimens have been machined out from the centre part of the larger specimens, see Figure 20(c).

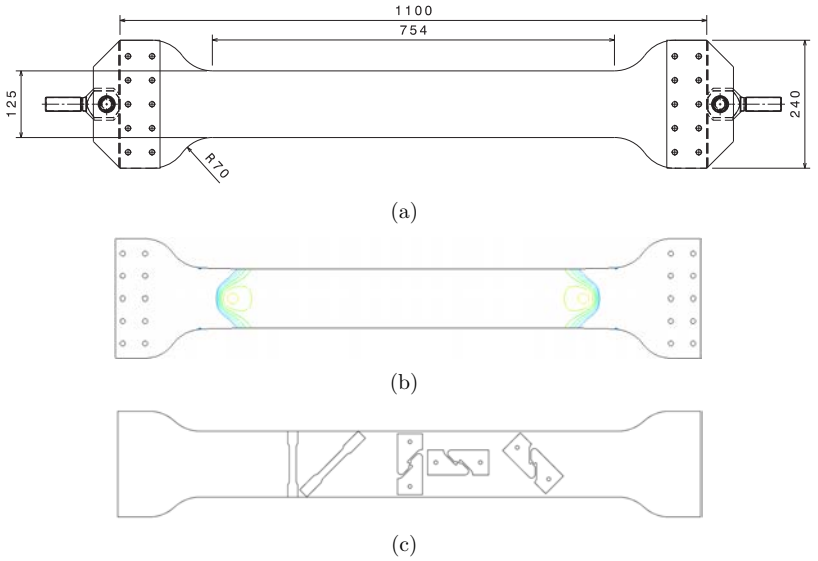

Figure 20: *a) Geometry of pre-strain specimen. b) Sketch including some cut out specimens. c) Distribution of longitudinal plastic strain. The iso-curves represent strain levels ranging from 9% to 11 % with 0.2% steps. Dimensions are given in mm.*

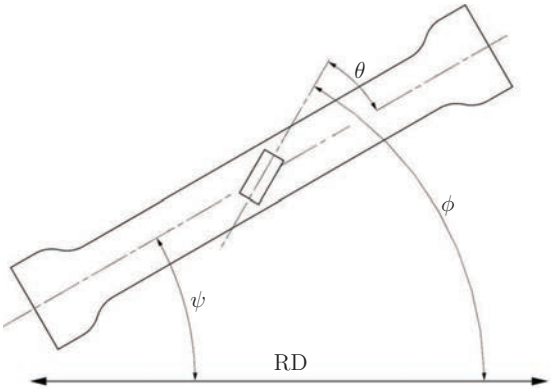

Figure 21: *Angles defining pre-strain directions, ψ, and directions of subsequent testings, $\phi = \psi + \theta$.*

Table 4: *Approximative plastic strains after pre-straining.*

Material	Docol 600DP				Docol 1200M			
Direction	RD		TD		RD		TD	
ε^p [%]	5	10	4.5	8	0.5	1	0.4	0.7

7.2 Tensile Test

The tensile tests have been used to represent the hardening up to diffuse necking and also to represent the anisotropy of the yield function and the kinematic hardening. Tensile test specimens according to Figure 22 have been performed in the $\phi = 0°$, $45°$ and $90°$ directions, where ϕ is the angle to the RD, see Figure 21, both for the as-received and the pre-deformed material specimens. During the tensile tests the load, elongation and width contraction were recorded. The elongation, ε_L, has been measured by an INSTRON 2620-601 extensometer with a gauge length of $L_0 = 12.5$ mm, and the width contraction, ε_W, has been measured with an MTS 632.19B-20 extensometer over the entire width of the specimen. The deformation was performed with a constant crosshead speed of 0.45 mm/min, which resulted in a strain-rate of approximately 10^{-4} s^{-1}. The anisotropy in yield stress and plastic flow were evaluated directly from the tensile tests of the as-received specimens. Also the hardening behaviour up to diffused necking is obtained directly from the experimental data. Numerical simulations and inverse modelling are used to identifying the kinematic hardening of the pre-strained materials.

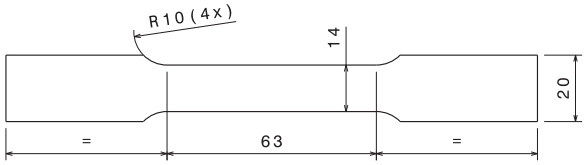

Figure 22: *Geometry of the tensile test with dimensions in mm.*

7.3 Simple Shear Test

The geometry of the simple shear test specimen used in this study is shown in Figure 23. The shear tests are performed on both as-received and on pre-deformed specimens in the $\phi = 0°$, $45°$ and $90°$ directions. The two attachments for the shear test have been in the form of a pin at both ends to prevent the specimens from rotational loading. In order to obtain a strain-rate of approximately 10^{-4} s^{-1}, the displacement rate of 0.03 mm/min has been used. The shear test results are used in combination with inverse modelling to gain an accurate description of the

hardening behaviour for large strains, to find the yieldsurface exponent, and to calibrate the Cockroft-Latham fracture model.

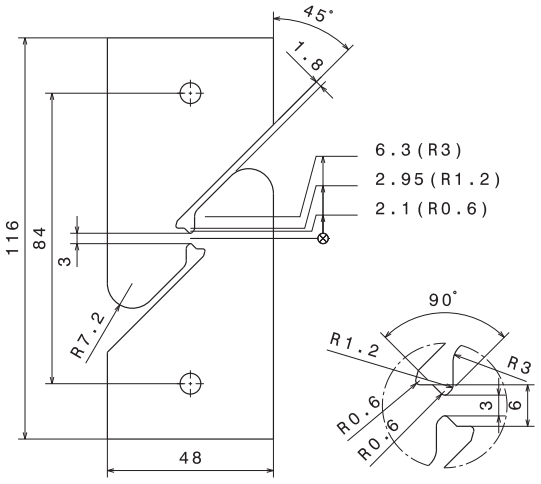

Figure 23: *Geometry of the shear specimen with dimensions in mm.*

7.4 Plane Strain Test

The geometry of the plane strain test (notched tensile test) is shown in Figure 24. Similar designs have been utilised in other studies, e.g. Lademo et al. (2008). The plane strain tests were performed in $\phi = 0°$, $45°$ and $90°$ directions, with a displacement rate of 0.06 mm/min. During the test the load, grip motion, width reduction and midsection elongation were measured. The latter was measured by an INSTRON 2620-601 extensometer width a gauge length of 23 mm, while the width reduction was measured by an MTS 632.19B-20 extensometer. The plane strain test is used in combination with inverse modelling in order to calibrate the Bressan-William fracture model.

7.5 Balanced Biaxial Test

A balanced biaxial bulge test was performed on the virgin materials. The pressure was applied with a punch made of silicon and a pattern of randomly placed dots was sprayed on the sheet surface. The specimen was video recorded by two cameras during the subsequent testing. The in-plane strains and the radius of the bulge were then evaluated from the recording of the pattern motion using an ARAMIS strain measurement system. Balanced biaxial tests have been used in order to obtain the stress and strain ratios r_b and k_b, respectively, cf. Sigvant et al. (2009).

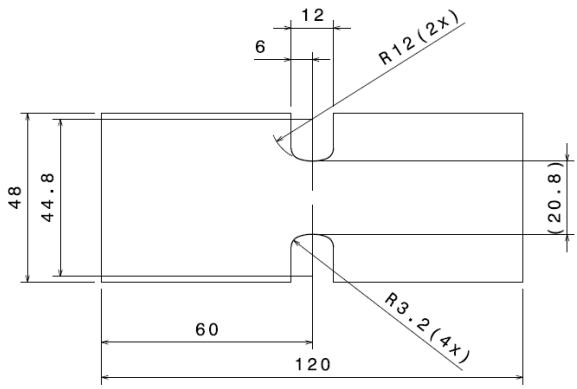

Figure 24: *Geometry of the plane strain specimen with dimensions in mm.*

7.6 Nakajima Test

A number of Nakajima tests, see ISO (2008), have been conducted in order to evaluate the failure behaviour. The tests were made on virgin material and the geometries, see Figure 25, were chosen so that the first quadrant ($\varepsilon_1 \geq 0$, $\varepsilon_2 \geq 0$) of the FLD was covered.

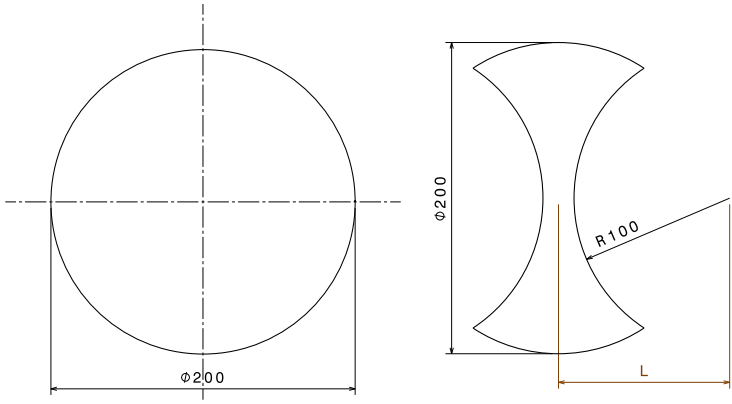

Figure 25: *Nakajima specimen geometry dimmensions in mm: (a) circular (b) with different waists (L=130,140,150,160,165 and 170 mm).*

The Nakajima tests were performed in an Interlaken ServoPress 150. The machine has a punch diameter of 100 mm and a load cell of 550 kN. The clamping force was limited to 700 kN and the punch motion was set to 1 mm/s. During the test the force and displacement of the punch was recorded. The specimens were

treated with three layers of oil and plastic film to reduce friction. Before the test a mesh with a 2 mm grid size was etched onto the specimens. The strains were then evaluated optically by an AutoGrid 4.1 Strain Analysis System, which used information from four cameras, each of which recorded 30 images per second during the test. The image just before the fracture was used to evaluate the limit strains. Since the image just before fracture is used, the strains may be well past the limit of localised necking. Therefore a method similar to the one described by Bragard et al. (1972) has been used to evaluate the limit strains at the onset of localised necking. This method is straightforward and the major and minor strain distributions on a few lines across the instability are considered. Afterwards the strains inside the localised region are excluded and a polynomial fit is adopted to the remaining strains. The maximum strain from this polynomial is chosen as the major strain limit, see Figure 26. For the minor strain a linear fit is performed at the location of the maximum.

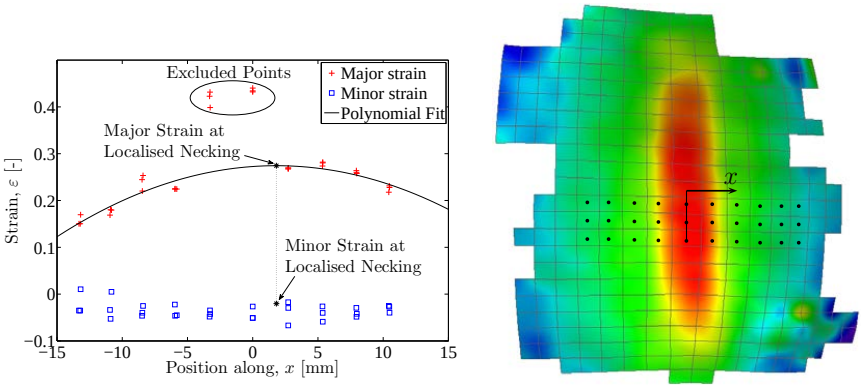

Figure 26: *Illustration of the Bragard et al. (1972) method; (a) polynomial fit to strains and (b) lines of elements across the localisation zone used for strain evaluation.*

8 Finite Element Modelling

Finite element analyses of the tensile, shear, plane strain and Nakajima experiments have been performed using LS-DYNA, see Hallquist (2009). All FE meshes have been produced in TrueGrid, see Rainsberger (2006). A non-local treatment of the fracture parameters is needed in order to reduce the mesh dependency. However, the C^0 continuity of the thickness across the element edges as obtained by the use of an extended shell element formulation contributes to a regularisation of the thickness strain, and thus reduces the mesh dependency. The introduction of the normal through-thickness stress, σ_{ND}, enables a C^0 continuity in the element formulation, cf. Borrvall and Nilsson (2003). However, the inclusion of the normal stress also introduces transversal shear stresses and strains, see Figure 27. The transversal shear stresses are not entering into the elasto-plastic constitutive model, but are updated elastically.

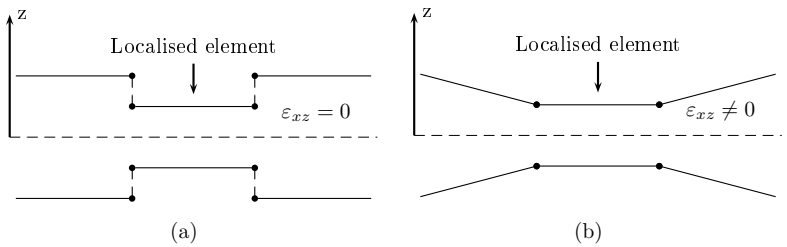

Figure 27: *Element formulation (a) ordinary plane stress element (b) a continuous thickness based element.*

The transversal shear stresses will prevent the localisation and will thus contribute to a stiffening effect. An improved result can be obtained by using an effective stress, which takes all stresses into account or by reducing the transversal shear stresses by a correction factor according to the theory of Reissner-Mindlin, see Hughes (2000). The latter method has been adopted here, i.e. the transversal shear stresses have been reduce by a shear correction factor, κ, according to

$$\sigma_{yz} = \kappa \frac{E}{2(1+\nu)} \varepsilon_{yz}, \quad \sigma_{zx} = \kappa \frac{E}{2(1+\nu)} \varepsilon_{zx} \tag{63}$$

where E and ν are the Young's modulus and Poisson's ratio, respectively. However, κ will also affect the hardening after diffused necking. Thus, the hardening after diffused necking has been modified compared to what was presented in Larsson et al. (2011) in order to maintain a good agreement between simulations and test results. The parameters of the hardening after necking and the shear correction factor, κ, have been obtained from inverse modelling of the tensile, shear and plane strain tests.

8.1 Pre-Straining

FE analyses of the tensile and shear experiments have been performed both for virgin and pre-strained specimens. The pre-straining operation, which produced the non-proportional strain paths, was made by stretching one single element to the strain levels shown in Table 4. The back-stress tensor, $\boldsymbol{\alpha}$, equivalent plastic strain, $\bar{\varepsilon}^p$, and fracture parameter, W, are subsequently mapped on the models of the small specimens used in the subsequent analyses, see Figure 28. Since the strain field from stretching one single element is mapped on to all elements of the model of each small specimen, no strain inhomogeneities will be present in the subsequent simulations.

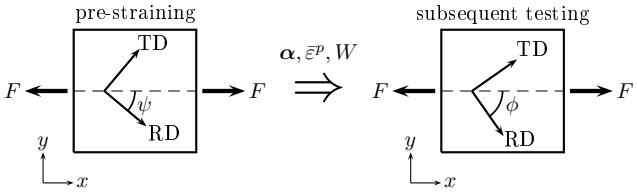

Figure 28: *One pre-strained element from which the backstress, $\boldsymbol{\alpha}$, equivalent plastic strain, $\bar{\varepsilon}^p$, and fracture parameter, W, are mapped to the models for the subsequent analyses.*

8.2 Tensile Test

The FE model of the tensile specimen is shown in Figure 29. It consists of about 5500 shell elements. The characteristic element size is approximately 0.5 mm. A good agreement between the stress-strain relationship simulation and tensile test results can be observed up to diffused necking, as reported in Larsson et al. (2011). By introducing a shear correction factor $\kappa = 0.05$ in the shell formulation and modifying the hardening curve after diffuse necking, improved agreement was obtained between the simulation and test results, even for the crosshead displacement after diffuse necking, see Figure 30.

Figure 29: *FE model of the tensile test specimen.*

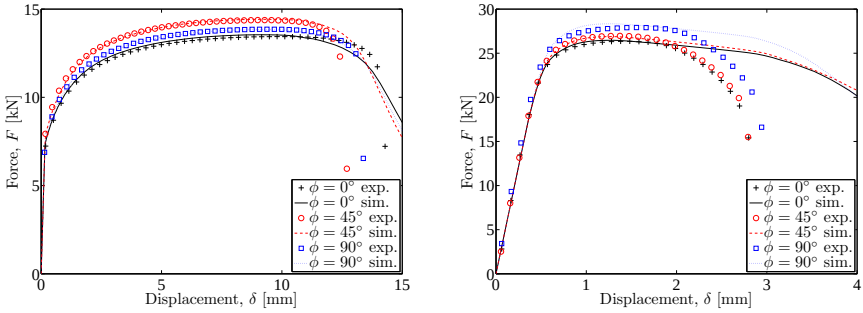

Figure 30: *Results from tensile test of virgin material in different material direction (a) Docol 600DP (b) Docol 1200M.*

8.3 Shear Test

The FE model of the shear specimen is shown in Figure 31. It consists of about 12500 shell elements. The characteristic element size in the shear zone is approximately 0.06 mm, see Figure 31(b). A good agreement between simulation results and the force-displacement relationships of the shear experiment was found after the correction of the shear factor and modification of the hardening curve, see Figure 32.

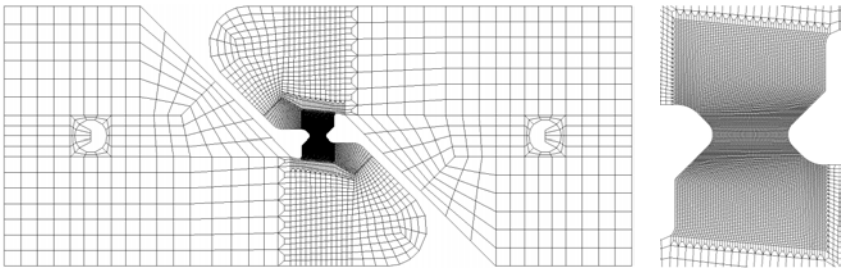

Figure 31: *(a) FE model of the shear specimen. (b) Details of the mesh in the shear zone.*

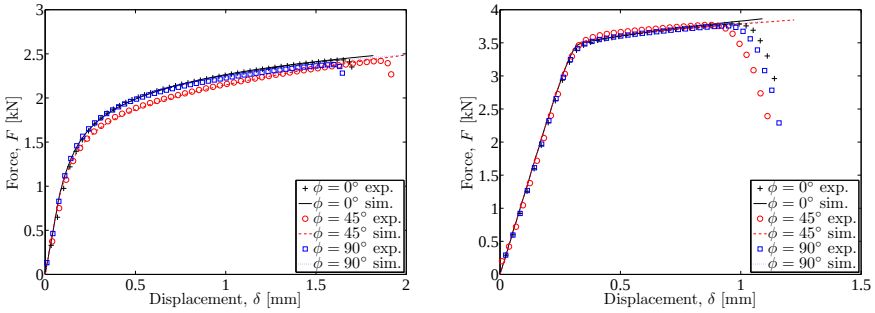

(a) (b)

Figure 32: *Results from shear test of virgin material in different material direction (a) Docol 600DP (b) Docol 1200M.*

8.4 Plane Strain Test

The FE model of the plane strain test specimen can be seen in Figure 33. The model consists of about 7900 shell elements. The element size in the centre of the specimen is approximately 0.2 mm. The C^0 continuous element formulation used through this work enabled an improved correspondence between FE simulation and experimental results compared to the conventional shell element formulation, see Figure 34. A good agreement between simulation results and the force-displacement relations for the plane strain tests was found, see Figure 35.

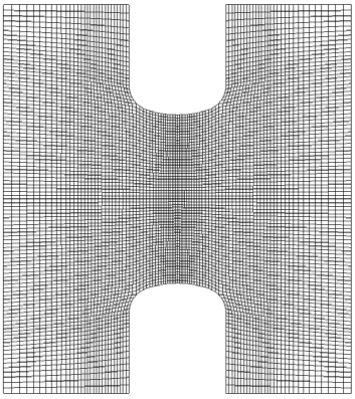

Figure 33: *FE model of the plane strain specimen.*

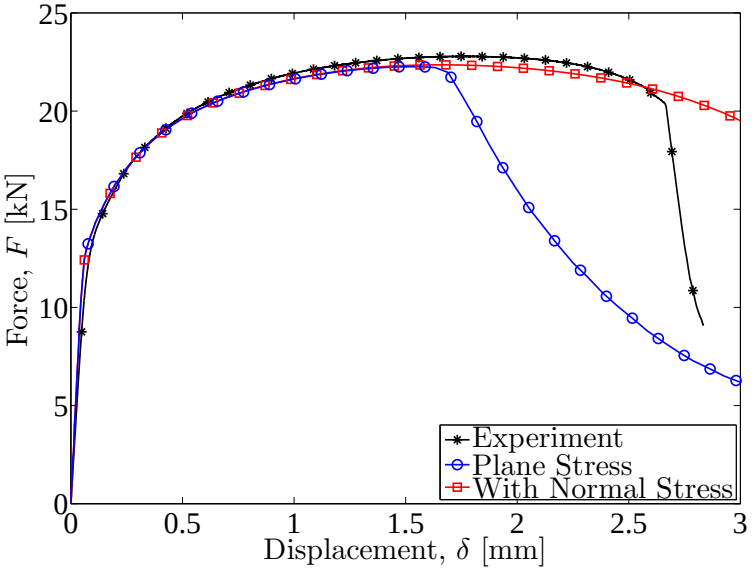

Figure 34: *Different element formulation used for simulations of the plane strain test.*

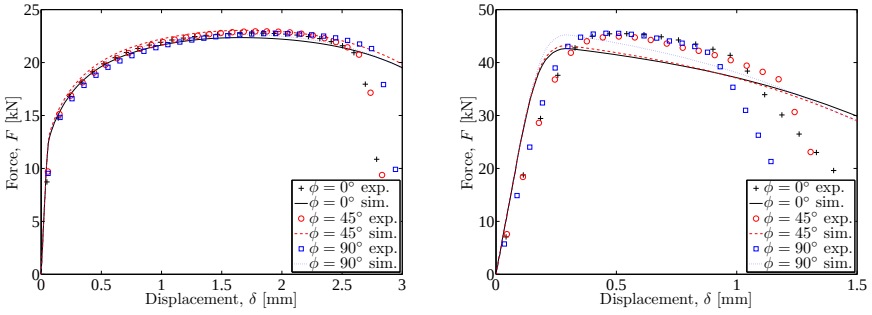

(a) (b)

Figure 35: *Results from plane strain test of virgin material in different material direction (a) Docol 600DP (b) Docol 1200M.*

8.5 Nakajima Test

The characteristic element size in the FE models of the Nakajima specimens was approximately 0.75 mm. Since the Nakajima tests are used for prediction of the failure behaviour, it was necessary to introduce a small disturbance of the thickness in order to capture the instability correctly. The thickness variation has here been given using the same method as for the patch discussed in Chapter 6. The Nakajima tests were used in order to evaluate the failure behaviour and a good agreement was obtained. However it has been seen that, the friction chosen between the specimen and punch surface in the simulation model is of a great importance in the prediction of the instability. The friction used in all simulation models has therefore been chosen such that the instability is predicted as close as possible to the specimen with a waist of 60 mm, see Figure 36.

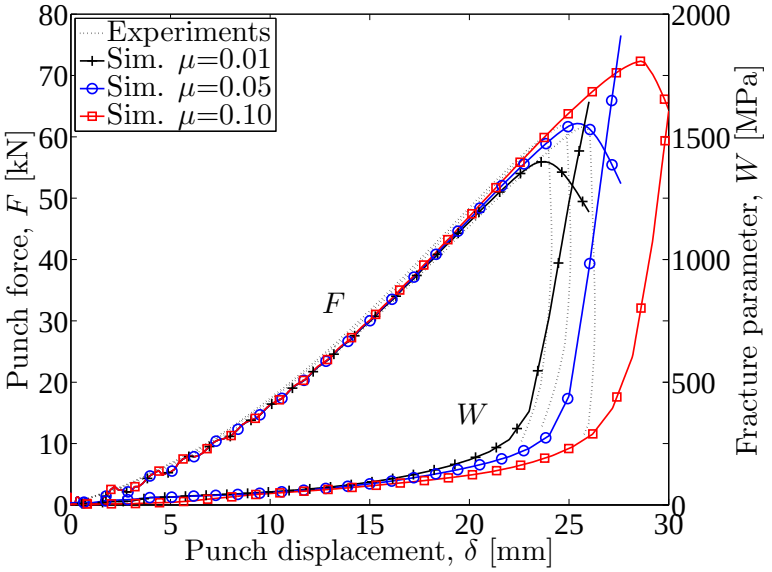

Figure 36: *Different friction for prediction of instability of the Nakajima test of Docol 600DP in RD with a waist of 60 mm.*

9 Conclusions and Discussion

One major objective of the proposed fracture models was that they should be easy to calibrate. Since both the models investigated in this thesis have only one material parameter, just one basic mechanical experiment and the corresponding FE simulation are sufficient for calibration. However, in several loading situations, it is hard to identify whether the fracture is initiated prior to the instability or after. In the plane strain test a localisation is observed before fracture, both in the FE simulations and the experiments. The fracture parameters calibrated from these experiments will then depend on how well the deformation is captured in the localised zone. It may be argued that the plane strain test should not be used for this calibration, since the instability arises before the fracture. The fracture model calibrated from the plane strain test can, since the instability arises before the fracture, be considered as an upper limit for the fracture within the FLD.

Even if one single experiment and one FE simulation are sufficient to calibrate each of the fracture models used in this study, one fracture parameter value was evaluated from specimens in all material directions of the virgin material. From the evaluation of these results it can be seen that there is a large variation in the parameters obtained from the different material directions and also within the different tests in the same direction. The behaviour of the material in different material directions cannot be predicted by the fracture models chosen for this study, since the fracture models adopted are isotropic, although the constitutive model is anisotropic. In order to predict the different fracture behaviour observed in different directions, an anisotropic fracture model is needed. The variation of the fracture appearance within the same material direction can be explained by the fact that the fracture is strongly influenced by inclusions and impurities within the material, and since these are located differently in different specimens the fractures will differ. It may thus be preferable to specify the fracture parameters with lower and upper limits rather than as a specific value.

Most of the Nakajima experiments and simulations show an instability before fracture. Consequently the prediction of this instability is very important. However, in this study the prediction of the instability is made by using the constitutive model and FE models with significantly dense meshes. In order to obtain a good prediction it is therefore necessary to carefully calibrate the material and fracture models before subsequent use. Since the shape of the yield surface, the hardening law and also the element formulation all affect the instability. Therefore it

is important to choose suitable mechanical experiments and element formulation for the calibration. The validation of the failure behaviour has been performed in experiments and FE simulations of the Nakajima tests. In the evaluation of the quality of the fracture and instability predictions, their representation is very important. One direct method is to compare the force-displacement curves from simulations and experiments directly. However, since the FLD is a commonly-used tool for failure prediction, it is also useful to represent failure predictions as FLC in an FLD. The curves representing the locus of different failures, i.e. ductile fracture, shear fracture and instability, are easy to interpret. Their representation of the strains from the experiments causing localisation is, however, not that trivial. There are many approaches on how to evaluate the forming limit. In experiments in this study, the deformation was monitored during the deformation, and thus the strains were captured close to the instance of fracture. However, the strains may then be well past the onset of localisation and the limit of instability needs to be evaluated using a different method. In some methods a few grid points outside the fracture zone are evaluated and the strains there are considered to be the limit. In this study the strains of failure are evaluated with a polynomial fit across the instability zone.

The results obtained from the failure prediction are generally in a good agreement with experiments. However, a large variation of fracture parameters is observed and an interval in its values is to be preferred, since some variation is always obtained in mechanical experiments. The variation in the mechanical experiments may be caused by a number of different factors such as variation in setup, variation in material and measurement error.

10 Review of Appended Papers

Paper I

A study of high strength steels undergoing non-linear strain paths - Experiments and modelling

This paper presents an evaluation of the constitutive behaviour, including plastic anisotropy and mixed isotropic-kinematic hardening of two high strength steels, Docol 600DP and Docol 1200M, during strain path changes. A series of tensile and shear tests was performed on both virgin and pre-strained materials. The initial anisotropy and work hardening parameters were obtained from tensile tests, shear tests and a bulge test of the virgin material, whereas the kinematic hardening parameters were identified by comparing numerical predictions to experimental results related to the pre-strained materials. Numerical predictions using the obtained parameters agree well with the experimental results, both in the case of proportional, and under non-proportional strain paths.

Paper II

Failure of high strength steel sheet - Experiments and modelling

Failure in thin sheet metal structures of ductile material is usually caused by one of, or a combination of, the following: ductile fracture, shear fracture or localised instability. In this paper the failure of the high strength steel Docol 600DP and the ultra high strength steel Docol 1200M is explored. The constitutive model used in this study includes plastic anisotropy and mixed isotropic-kinematic hardening. For modelling of the ductile and shear fracture the models presented by Cockroft-Latham and Bressan-Williams have been used. The instability phenomenon is described by the constitutive law and the finite element (FE) models. For calibration of the failure models and validation of the results, an extensive experimental series has been conducted including shear tests, plane strain tests and Nakajima tests. The geometries of the Nakajima tests have been chosen so that the first

quadrant of the forming limit diagram (FLD) were covered. The results are presented both in an FLD and using prediction of force-displacement response of the Nakajima test employing element erosion during the FE simulations. The classical approach for failure prediction is to compare the FE simulations with experimental determined forming limit curves (FLC). Here phenomenological models have been used which show promising results. The benefit of using phenomenological models is the ability to follow failure behaviour for more complex loading paths.

Bibliography

Aretz, H., 2004. Numerical restrictions of the modified maximum force criterion for prediction of forming limits in sheet metal forming. Modelling and Simulation in Materials Science and Engineering 12 (4), 677–692.

Aretz, H., 2005. A non-quadratic plane stress yield function for orthotropic sheet metals. Journal of Materials Processing Technology 168 (1), 1 – 9.

Askeland, D. R., 1998. The Science and Engineering of Materials. Nelson Thornes Ltd, Sheffield.

Bai, Y., Wierzbicki, T., 2008. A new model of metal plasticity and fracture with pressure and Lode dependence. International Journal of Plasticity 24 (6), 1071 – 1096.

Banabic, D., Barlat, F., Cazacu, O., Kuwabara, T., 2010. Advances in anisotropy and formability. International Journal of Material Forming 3, 165–189.

Bao, Y., Wierzbicki, T., 2004. On fracture locus in the equivalent strain and stress triaxiality space. International Journal of Mechanical Sciences 46 (1), 81 – 98.

Belytschko, T., Liu, W. K., Moran, B., 2000. Nonlinear Finite Elements for Continua and Structures. Wiley, Chichester.

Borrvall, T., Nilsson, L., 2003. Revision of the implementation of material 36 in LS-DYNA. Engineering Reaserch Nordic AB, Linköping, private communication.

Bragard, A., Baret, J.-C., Bonnarnes, H., 1972. A simplified technique to determine the FLD at the onset of necking. Report no. 33, Rapport Centre de Recherche de la Mètallurgie, Liège.

Bressan, J., Williams, J., 1983. The use of a shear instability criterion to predict local necking in sheet metal deformation. International Journal of Mechanical Sciences 25 (3), 155–168.

Cockroft, M. G., Latham, D. J., 1968. Ductility and the workability of metals. Journal of the Institute of Metals 96, 33–39.

Dieter, G. E., 1986. Mechanical Metallurgy. McGraw-Hill, New York.

Frederick, C., Armstrong, P., 2007. A mathematical representation of the multiaxial Bauschinger effect. Materials at High Temperatures 24 (1), 1–26.

Fyllingen, O., Hopperstad, O., Lademo, O.-G., Langseth, M., 2009. Estimation of forming limit diagrams by the use of the finite element method and Monte Carlo simulation. Computers and Structures 87 (1-2), 128 – 139.

Gurson, A., 1977. Continuum theory of ductile rupture by void nucleation and growth: Part I - yield criteria and flow rules for porous ductile media. Journal of Engineering Materials and Technology 99 (1), 2 – 15.

Hallquist, J., 2009. LS-DYNA Theory Manual. Livermore Software Technology Corporation, Livermore.

Han, H. N., Kim, K.-H., 2003. A ductile fracture criterion in sheet metal forming process. Journal of Materials Processing Technology 142 (1), 231 – 238.

Hill, R., 1952. On discontinuous plastic states, with special reference to localized necking in thin sheets. Journal of the Mechanics and Physics of Solids 1 (1), 19 – 30.

Hollomon, J. H., 1945. Tensile deformation. Transaction of the American Institute of Mining, Metallurgical and Petroleum Engineers 162, 268–290.

Hooputra, H., Gese, H., Dell, H., Werner, H., 2004. A comprehensive failure model for crashworthiness simulation of aluminium extrusions. International Journal of Crashworthiness 9 (5), 449 – 63.

Hora, P., Tong, L., Reissner, J., 1996. A prediction method for ductile sheet metal failure in FE-simulation. Proceedings of the 3'rd International Conference Numisheet'96, Dearborn, Michigan, 252–256.

Hosford, W., Cadell, R., 1993. Metal Forming Mechanics and Metallurgy. Prentis-Hall, New York.

Hughes, T. J. R., 2000. The Finite Element Method - Linear Static and Dynamic Finite Element Analysis. Dover Publications, Mineola, New York.

ISO, 2008. Metallic materials -sheet and strip - determination of forming limit curves - Part 2: Determination of forming limit curves in the laboratory. 12004-2:2008, Austrian Standards Institute, Wien.

Johnson, G. R., Cook, W. H., 1983. Fracture characteristics of three metals subjected to various strains, strain rates, temperatures and pressures. Seventh International Symposium on Ballistics, Hague, 1–7.

Johnson, G. R., Cook, W. H., 1985. Fracture characteristics of three metals subjected to various strains, strain rates, temperatures and pressures. Engineering Fracture Mechanics 21 (1), 31 – 48.

Krauss, G., 2005. Steels Processing, Structure, and Preformance. ASM International Materials Park, Ohio.

Lademo, O.-G., Berstad, T., Hopperstad, O. S., Pedersen, K. O., 2004a. A numerical tool for formability analysis of aluminium alloys. Part I: Theory. Steel Grips 2, 427–432.

Lademo, O.-G., Pedersen, K., Berstad, T., Furu, T., Hopperstad, O., 2008. An experimental and numerical study on the formability of textured AlZnMg alloys. European Journal of Mechanics - A/Solids 27 (2), 116 – 140.

Lademo, O.-G., Pedersen, K. O., Berstad, T., Hopperstad, O. S., 2004b. A numerical tool for formability analysis of aluminium alloys. Part II: Experimental validation. Steel Grips 2, 433–437.

Larsson, R., Björklund, O., Nilsson, L., Simonsson, K., 2011. A study of high strength steels undergoing non-linear strain paths - experiments and modelling. Journal of Materials Processing Technology 211, 122–132.

Lemaitre, J., 1985. A continuous damage mechanics model for ductile fracture. Journal of Engineering Materials and Technology 107, 83–89.

Lemaitre, J., Chaboche, J.-L., 1990. Mechanics of Solid Materials. Cambridge University Press, Cambridge.

Marciniak, Z., Kuczynski, K., 1967. Limit strains in the processes of stretch-forming sheet metal. International Journal of Mechanical Sciences 9 (9), 609–620.

Olsson, K., Gladh, M., Hedin, J.-E., Larsson, J., 2006. Microalloyed high-strength steels. Advanced Materials and Processes 164 (8), 44–46.

Opbroek, E. G., 2009. Advanced high strength steel application guidelines. Tech. Rep. WorldAutoSteel.

Oyane, M., Sato, T., Okimoto, K., Shima, S., 1980. Criteria for ductile fracture and their applications. Journal of Mechanical Working Technology 4 (1), 65 – 81.

Rainsberger, R., 2006. TrueGrid User's Manual. XYZ Scientific Applications, Inc., Livermore.

Shinozuka, M., Deodatis, G., 1996. Simulation of multi-dimensional Gaussian stochastic fields by spectral representation. Applied Mechanics Reviews 49, 29–53.

Sigvant, M., Mattiasson, K., Vegter, H., Thilderkvist, P., 2009. A viscous pressure bulge test for the determination of a plastic hardening curve and equibiaxial material data. International Journal of Material Forming 2 (4), 235–242.

Swift, H. W., 1952. Plastic instability under plane strain. Journal of the Mechanics and Physics of Solids, 1, 1–18.

Teirlinck, D., Zok, F., Embury, J., Ashby, M., 1988. Fracture mechanism maps in stress space. Acta Metallurgica 36 (5), 1213 – 1228.

Voce, E., 1948. The relationship between stress and strain for homogenus deformation. Journal of the Institute of Metals 74, 537–562.

Wierzbicki, T., Bao, Y., Lee, Y.-W., Bai, Y., 2005. Calibration and evaluation of seven fracture models. International Journal of Mechanical Sciences 47 (4-5), 719 – 743.

Wilkins, M. L., Streit, R. D., Reaugh, J. E., 1980. Cumulative-strain-damage model of ductile fracture: Simulation and prediction of engenering fracture tests. Tech. Rep. Lawrence Livermore National Laboratory, Livermore.